12-1-2022

Along Strike Tectonic Evolution of the Neogene Bermejo Foreland Basin and Eastern Precordillera Thrust Front, Argentina (30-32ºs)

Zoey Catherine Plonka

ALONG STRIKE TECTONIC EVOLUTION OF THE NEOGENE BERMEJO FORELAND BASIN AND EASTERN PRECORDILLERA THRUST FRONT, ARGENTINA (30-32ºS)

By

Zoey Catherine Plonka

Bachelor of Science- Earth and Environmental Science
University of Michigan, Ann Arbor
2019

A thesis submitted in partial fulfillment
of the requirements for the

Master of Science – Geoscience

Department of Geoscience
College of Sciences
The Graduate College

University of Nevada, Las Vegas
December 2022

UNLV | GRADUATE COLLEGE

Thesis Approval

The Graduate College
The University of Nevada, Las Vegas

November 3, 2022

This thesis prepared by

Zoey Catherine Plonka

entitled

Along Strike Tectonic Evolution of the Neogene Bermejo Foreland Basin and Eastern Precordillera Thrust Front, Argentina (30-32ºs)

is approved in partial fulfillment of the requirements for the degree of

Master of Science – Geoscience
Department of Geoscience

Tomas Capaldi, Ph.D
Examination Committee Chair

Michael Wells, Ph.D.
Examination Committee Member

Kevin Konrad, Ph.D
Examination Committee Member

Carlos Dimas, Ph.D.
Graduate College Faculty Representative

Alyssa Crittenden, Ph.D.
Vice Provost for Graduate Education & Dean of the Graduate College

ABSTRACT

The Bermejo retroarc foreland basin system formed in flexural response to Miocene crustal thickening in the Andean orogenic system, specifically, the eastward propagation of the Precordillera fold-thrust belt and the basement-involved uplift of the Sierras Pampeanas. Previous work in the area has mainly focused on the mechanisms and expression of flat slab subduction and the structural geometry of the basement-involved Sierras Pampeanas and east-vergent Precordillera fold-thrust belt at depth. Much of this work has furthered the understanding of Bermejo basin evolution north of 31ºS, however debate still exists whether the N-S trending Bermejo basin evolved synchronously or asynchronously through time. An in-depth, along-strike analysis of the Bermejo basin is required to determine whether or not the basin evolved synchronously. Our study seeks to constrain the along-strike Neogene tectonics of the Eastern Precordillera via well exposed Bermejo basin deposits through integration of new stratigraphic, detrital zircon U-Pb geochronology provenance, and detrital apatite low temperature thermochronology datasets from southern Bermejo basin. New data from two <2 km thick Neogene stratigraphic sections in southern Bermejo basin constrain deposition between *ca*. 13-5 Ma with dominant fluvial-lacustrine mudstones, siltstones and sandstones that transition into fluvial-alluvial fan conglomerate facies tracking the eastward migration of deformation. New detrital apatite thermochronology ages from the base of the measured sections record a mean age of *ca*. 6 Ma, suggesting two temporally distinct deformation events along-strike of the Bermejo basin. When we compare our new data with published data from northern Bermejo, we observe a north to south: (1) decrease in stratigraphic thicknesses, and (2) increase in exhumation ages along strike. This study utilizes newly collected data in comparison with published data to constrain along-strike variability of Precordillera thrust-front evolution and Bermejo basin development.

ACKNOWLEDGMENTS

Now that I have completed my thesis, and I can look back upon the experience fondly, I would like take a moment to acknowledge the group of people who supported me throughout this process. I must start with Dr. Tomas Capaldi, who although is a rookie in the role of advising grad students, was able to offer an immense amount of personal support, geologic knowledge, and countless great song recommendations. Through my time spent working with Tomas, I have become a better (and more confident) scientist and writer, and I will always be grateful for the things I've learned from him. Tomas is in the early stages of his (what I am sure will be long and successful) career as a researching professor, and I can only hope that he will always remember his first two students fondly. Speaking of which, I must also thank fellow MS student James Duncan. In our early and modest research group here at UNLV, Tomas forced James and I to discuss papers together, assist each other in the field, and edit each other's work – what wasn't forced but simply a side effect of this time spent was the lifelong friendship that was built between the two of us. Thank you James, Kamay, and Caspian for allowing me to be a part of your family (& all those wonderful homecooked meals) while mine was many miles away. On that note, thank you to my family, who never seemed to doubt that I was going to do it. I believe that I am a culmination of all of my life experiences, and I like to think that those early, beloved family camping trips shaped me into the outdoorsy, curious, rock-loving person I am today.

I would like to thank my committee members who offered guidance and support throughout this process. Dr. Michael Wells and Dr. Kevin Konrad are two immensely knowledgeable geologists and I thank them for their insight and thought-provoking questions. I thank all of the folks down at the University of Texas UTChron facilities, especially Dr. Daniel Stockli, Rudra Chatterjee, and Zachary Foster-Baril. Dr. Margo Odlum was our chief

thermochronologist, and I thank her for the time spent reviewing my data, helping me to understand said data, and the general support that she offered throughout this process. Dr. Chris DeFelice here at the Nevada Plasma Facilities Laboratory helped us retrieve our geochronology data, I thank him for his time and expertise. I am grateful to have been a part of inception of the Cest LV research group, headed by Dr. Tomas Capaldi and Dr. Margo Odlum. While I am surely thankful for all the time spent practicing talks and discussing progress during Cest LV group meetings, I am even more thankful for the fun times and that above all, that we always seemed to start our meetings off with a good laugh. I am so thankful for all the wonderful friends I made while at UNLV.

As I reflect on all the people who made this journey possible, I must mention my partner and biggest supporter, Nathan Carey. Nathan offered me endless love and support during this process. He was always willing to sit and discuss my data, my thoughts, my questions. He reviewed figures, text, and listened to countless practice talks. Nathan did all of this while *also* writing a master's thesis. On our busiest, most stressful days, we daydreamed about how great things were going to be when this was all said and done. We are dangerously close, a little anxious, and incredibly hopeful. I cannot wait to see what comes next. I am thankful to have had this opportunity.

TABLE OF CONTENTS

LIST OF TABLES

LIST OF FIGURES

1. INTRODUCTION

The Pampean flat slab segment of the central Andean orogenic system (Fig. 1) represents a region where the Nazca plate is subducted below the South American plate sub-horizontally (Barazangi & Isacks, 1976, 1979; Ramos et al., 2002). This region of flat-slab subduction is recognized by a spatial gap of active arc magmatism and a foreland basin region partitioned by the basement involved uplifts of the Sierras Pampeanas, which has been suggested to be driven largely by subduction of the Juan Fernandez ridge (Barazangi & Isacks, 1976; Jordan et al., 1983; Ramos et al., 2002; Alvarado et al., 2009; Ramos & Folguera, 2009). The Bermejo basin is situated in the foreland of the Andean orogenic system, and as such acts as an active record of magmatism and deformation associated with changes in subduction dynamics over the past ~20 Myr (e.g. Jordan et al., 2001; Verges et al., 2001; Levina, et al., 2014; Fosdick et al., 2015; Capaldi et al., 2020; Stevens-Goddard et al., 2021). Andean deformation propagated eastward during the past 20 Myr and is collocated with migration of magmatism towards the craton as the Nazca slab flattened and induced thermal weaknesses in the crust (Kay and Abbruzzi, 1996; Cristallini and Ramos, 2000; Kay and Mpodozis, 2001; Ramos et al., 2002; Ramos and Folguera, 2009; Allmendinger and Judge, 2014; Capaldi et al., 2021; Mackaman-Lofland et al., 2020; 2022). The thick-skinned Sierras Pampeanas basement-involved ranges partitioned the once continuous foreland basin during the Miocene (*ca*. 5-0 Ma) forming a broken foreland basin system (Fig. 1; Malizia et al., 1995; Jordan and Allmendinger, 1986; Jordan et al., 2001; Ortiz et al., 2015; 2021; Horton et al., 2022). Research in the Pampean flat-slab region has furthered our understanding of (1) the drivers and consequences of flat slab subduction at convergent plate boundaries, (2) the development and evolution of broken-foreland basin systems, and (3) the usefulness of well-preserved basin stratigraphy in understanding Andean tectonics. Nevertheless, the spatial trends in deformation

along strike of the Neogene Bermejo basin and associated thrust front structures remain unresolved.

The well-preserved Cenozoic basin stratigraphy of the northern Bermejo basin (north of 31°S) has been well documented as a recorder of deformation in the Andean hinterland and Precordillera fold-thrust belt since at least *ca*. 20 Ma (Johnson et al., 1986; Beer and Jordan, 1989; Jordan et al., 1993, 1997, 2001; Fernandez et al., 1996; Milana et al., 2003; Fosdick et al., 2015, Capaldi et al., 2020; Mackaman-Lofland et al., 2022). Uncertainties remain in regards to the spatial and temporal along-strike evolution of deformation and associated foreland basin development. Andean mountain building has been proposed to be asynchronous from north to south, indicating deformation and foreland basin development tracks spatially and temporally with the subduction of the Juan Fernandez ridge and associated flat slab geometry (Beer et al., 1989; Jordan et al., 1993; 2001; Ramos and Folguera, 2009; Verges et al., 2001). Geophysical modeling of the Juan Fernandez ridge suggests that the asperity migrated south along the South American margin for the past 25 Myr with subduction initially occurring at 20°S in the Bolivian orocline and migrating to its current position of 32°S by 12 Ma (Yanez et al, 2001; Kay and Coira, 2009). However, recent low-temperature thermochronology results along strike in the Precordillera fold-thrust belt recorded a spatially synchronous exhumation event around 12-9 Ma (Levina et al., 2014). The Precordillera is classified as an east-directed, thin-skinned fold-thrust belt which includes the enigmatic, west-directed frontal thrust system of the Eastern Precordillera abutting the foreland (Fig. 2). Reconstructions of the tectonic history of the Eastern Precordillera show large uncertainties in terms of when deformation initiated along strike, and the kinematic relationships between the trailing Central Precordillera ramp-flat thrust system and the east flanking Sierras Pampeanas basement-involved uplifts. A better understanding of the timing of deformation,

exhumation and stratigraphic unroofing patterns of the Eastern Precordillera is critical to understanding the upper-crustal response to flat-slab subduction and broken foreland basin evolution. Previous work in the northern portion of the Bermejo basin has constrained Neogene deposition and deformation associated with the contemporaneously advancing Precordillera thrust-front (Fig. 2; e.g. Beer and Jordan, 1989; Capaldi et al., 2020; Fosdick et al., 2015; Levina et al., 2014; Jordan et al., 1993, 1997, 2001; Milana et al., 2003), however datasets are lacking for the southern Bermejo basin. We argue that an along strike analysis of the depositional and deformational history between 30-32ºS is crucial to understanding the variability that exists in the evolution of the Precordillera fold-thrust belt and the development of the associated foreland basin.

Our study seeks to constrain the along-strike Neogene tectonics of the Bermejo basin and Eastern Precordillera through the integration of new stratigraphic, detrital zircon U-Pb geochronology provenance, and detrital apatite low-temperature thermochronology datasets from the southern Bermejo basin (Fig. 2). The Bermejo basin deposits are found along a well-exposed outcrop belt that overlies the Eastern Precordillera structures, providing an ideal system to conduct an along-strike analysis of both Precordilleran deformation and the closely associated basin evolution. Temporal constraints in the northern Bermejo suggest a depositional history initiating around *ca*. 24-18 Ma (Johnson et al., 1986; Fosdick et al., 2015; Milana et al., 2003; Capaldi et al., 2020) and exhumation initiating *ca*. 2 Ma (Fosdick et al., 2015). By integrating new geo- and thermochronologic datasets in the southern Bermejo with published datasets from northern Bermejo, we can begin to assess whether: (1) the Bermejo basin developed as a continuous flexural basin or was spatially discontinuous along strike, and (2) if the along-strike deformation of basin deposits was coeval or diachronous. Two new stratigraphic sections in the southern Bermejo basin were measured and described in detail. Measurements of paleocurrents and conglomerate clast

compositions were taken, samples were collected from each section for detrital zircon geochronology for chronostratigraphy and sediment provenance, and basal sandstones were collected for apatite helium thermochronologic analyses to track the thermal evolution of the basin during subsidence and exhumational cooling. These new sedimentological and geo-thermochronologic constraints from the southern Bermejo basin are compared against existing data from the northern Bermejo basin to track the along-strike variations and complexities in thrust-front evolution and foreland basin development.

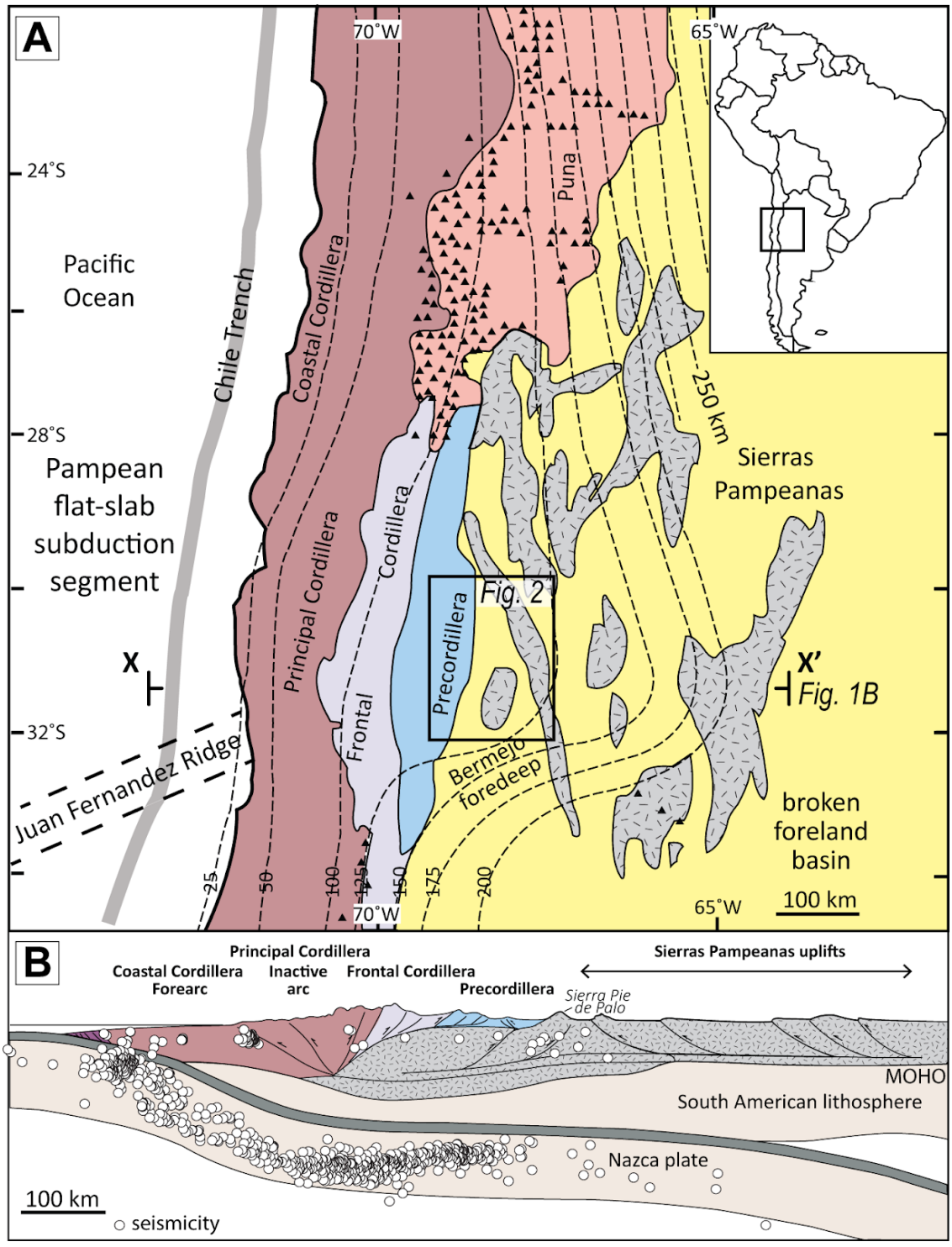

Figure 1: Tectonic setting of the southern Central Andes. (A) Geologic map of major tectonic provinces in the Pampean flat-slab segment of western Argentina and northern Chile, Quaternary Andean arc volcanic centers (black triangles), contoured Benioff zone depths (in km) to the subducted Nazca plate (dashed contour lines), and cross-section X-X' location (after Ramos et al., 2002). (B) East-west crustal cross section showing various Andean ranges and pro-posed basement terranes of the South American plate (after Bellahsen et al., 2016). Active seismicity (white circles) defines major crustal structures and Nazca plate geometry (Alvarado et al., 2009).

2. GEOLOGIC BACKGROUND

The Andean foreland of west-central Argentina is located within the Pampean flat slab segment of the Nazca-South American plate boundary where the thin-skinned Precordillera and basement-involved Sierras Pampeanas structural provinces spatially overlap (Fig. 1; Jordan and Allmendinger, 1986; Horton et al., 2022). The south-central Andes (30-32°S) is divided into five distinct tectonic provinces (Figs. 1 and 2): (1) the Andean arc and hinterland, (2) Central Precordillera, (3) Eastern Precordillera, (4) Sierras Pampeanas, and (5) Bermejo foreland basin.

The Andean arc and hinterland region along the Chile-Argentina border is composed of a suite of Jurassic-Miocene volcanic and volcaniclastic rocks deformed within the thin-skinned Principal Cordillera that overlie the Carboniferous-Triassic igneous rocks of the Frontal Cordillera (Fig. 1; Cristallini and Ramos, 2000; Mackaman-Lofland et al., 2019). The Frontal Cordillera consists of basement-involved structures that exhumed a >3 km thick assemblage of Carboniferous-Triassic igneous rocks, potentially as early as 30 Ma (Lossada et al., 2017; Mackaman-Lofland et al., 2022). Igneous rocks of the Frontal Cordillera include the Elqui-Limarí and Chollay batholiths, Choiyoi Group granodiorites, andesitic/rhyolitic lavas, and pyroclastic rocks (Mpodozis and Kay, 1992; Sato et al., 2015). The Manantiales and Calingasta-Iglesia hinterland basins flank the Frontal Cordillera and record deposition between 22 to 14 Ma (Pinto et al., 2018; Capaldi et al., 2020; Mackaman-Lofland et al., 2020; Podesta et al., 2022).

The Central Precordillera is separated from the Andean Hinterland by the north-trending Iglesias-Calingasta-Uspallata basin (Beer at al., 1990). The Central Precordillera thrust belt accommodated a majority of the Andean retroarc shortening (>100 km of E-W shortening) by imbricate thrusting above a ~4-12 km deep decollement within Ordovician-Lower Devonian strata

(Von Gosen, 1992; Allmendinger and Judge, 2014). Precordillera structures involve six east-verging faults and associated fault-propagation folds that deform Paleozoic and overlying Cenozoic foreland basin cover strata (Allmendinger et al., 1990; Jordan et al., 1993). Stratigraphy in the Central Precordillera consists of Cambrian-Ordovician carbonates (Don Polo Formation), siliciclastics and a sedimentary mélange (Los Sombreros Formation) that are unconformably covered by Silurian-Devonian marine rocks (Punta Negra Formation) (Von Gosen, 1992; Mardonez et al., 2020). Structural and sedimentologic analyses of basin deposits found within the Central Precordillera as well as Bermejo foreland basin deposits indicate deformation and erosion initiated around 18-16 Ma with a major phase of exhumation at 12-9 Ma (Beer and Jordan, 1989; Jordan et al., 1990, 1993; Allmendinger and Judge, 2014; Levina et al., 2014; Fosdick et al., 2015; Mackaman-Lofland et al., 2022).

The Eastern Precordillera is a nearly 400 km long thrust front that abuts the Bermejo foreland basin. The Cambrian-Ordovician carbonate rocks of the Eastern Precordillera comprise the sedimentary cover overlying Grenvillian basement of the Cuyania terrane (Astini et al., 1995; Keller, 1999; Ortiz et al., 2015; Thomas et al., 2015). Paleontological and stratigraphic data suggest that this exotic terrane represented a conjugate rift pair of the Laurentian margin, which then accreted to Gondwana in the Ordovician during the Famatinian Orogeny (Ramos et al., 1986; Astini et al., 1995; Keller, 1999; Thomas et al., 2015). Previous work in the northern Eastern Precordillera (~30ºS) identified the controlling structure as a hybrid thin- and thick-skinned triangle zone, where the Central Precordillera represents an east-verging, thin-skinned thrust system and the Eastern Precordillera represents a west-verging basement-involved thrust linked to the Sierras Pampeanas (Zapata and Allmendinger, 1996; Mardonez et al., 2020). The west-verging thrusts of the southern Eastern Precordillera (at the Rio San Juan section) have been interpreted as

a back-thrust zone to the Argentine Precordillera, likely reflecting reactivation of older reverse faults within the Eastern Precordillera (Von Gosen, 1992; Meigs et al., 2006).

The Bermejo foreland basin is structurally partitioned by the Sierras Pampeanas, which are predominately north trending ranges uplifted along moderately to highly dipping basement-involved thrusts (Gonzalez Bonorino, 1950; Ramos et al., 2002). The western Sierras Pampeanas include Sierra Valle de Fertil and Sierra Pie de Palo, which place Precambrian-Ordovician igneous and metamorphic rocks against Neogene foreland basin deposits (Ortiz et al., 2015; 2021). The Mesoproterozoic basement assemblages exposed throughout the Sierras Pampeanas record poly-phase deformation attributed to Pampean (555-515 Ma) and Famatinian (495-460 Ma) orogenesis during accretion of Laurentian terranes to the Gondwanan margin (Casquet et al., 2001; Ramos, 2004; Mulcahy et al., 2011; 2014; Tholt et al., 2021). Low temperature thermochronology and broken basin record from the western Sierras Pampeanas ranges record Andean deformation around 5 Ma (Ortiz et al., 2015; 2021; Capaldi et al., 2020). Presence of older Permian-Cretaceous cooling ages could be a result of protracted and limited cooling in the last 20 Myr or the existence of topographic relief prior to reverse faulting and flattening of the Nazca slab during the Andean Orogeny (Ortiz et al., 2015; 2021). The Eastern Precordillera and Sierras Pampeanas domains remain active today (Meigs et al., 2006; Ortiz et al., 2015, 2021; Rimando and Schoenbohm, 2020) evident by high seismic activity in the surrounding regions (Alvarado and Beck, 2006; Hartzell, 1996; Ortiz et al., 2015; Verges et al., 2007). The seismic activity in this region has resulted in the most devastating earthquakes in Argentina history (Alvarado and Beck, 2006; Langer and Hartzell, 1996).

The Bermejo foreland basin lies between the Precordillera fold-thrust belt and Sierra Valle de Fertil and can be divided into: (1) northern Bermejo basin which lies north of 31° S and includes

the previously studied Huaco (Johnson et al., 1986; Jordan et al., 2001, Fosdick et al., 2015) and Mogna (Milana et al., 2003; Capaldi et al., 2020) depocenters, and (2) southern Bermejo basin, situated south of 31° S and includes the newly studied Ullum (Bercowski et al., 1987; Contreras et al., 2019) and Villicum depocenters (Fig. 2). The Villicum section is an outcrop belt exposed along drainages off of Sierra Villicum, north of La Laja. The section was measured utilizing three to five-meter-high outcrops exposed within small incised stream channels. The Ullum section is well exposed along the Rio San Juan downstream of the Ullum Reservoir (Fig. 2), northeast of the City of San Juan and was able to be measured nearly continuously along strike. The Neogene stratigraphy of the Villicum and Ullum sections defines a regional angular unconformity with the underlying Paleozoic rocks (Silurian El Rinconada Formation at Villicum and Cambrian La Lajas Formation at Ullum; Fig. 2). Exposure and land accessibility became difficult to navigate near the top of the measured sections and therefore stratigraphic thicknesses presented likely do not represent true stratigraphic thickness. Estimated true thicknesses of both stratigraphic sections is roughly 1800 meters.

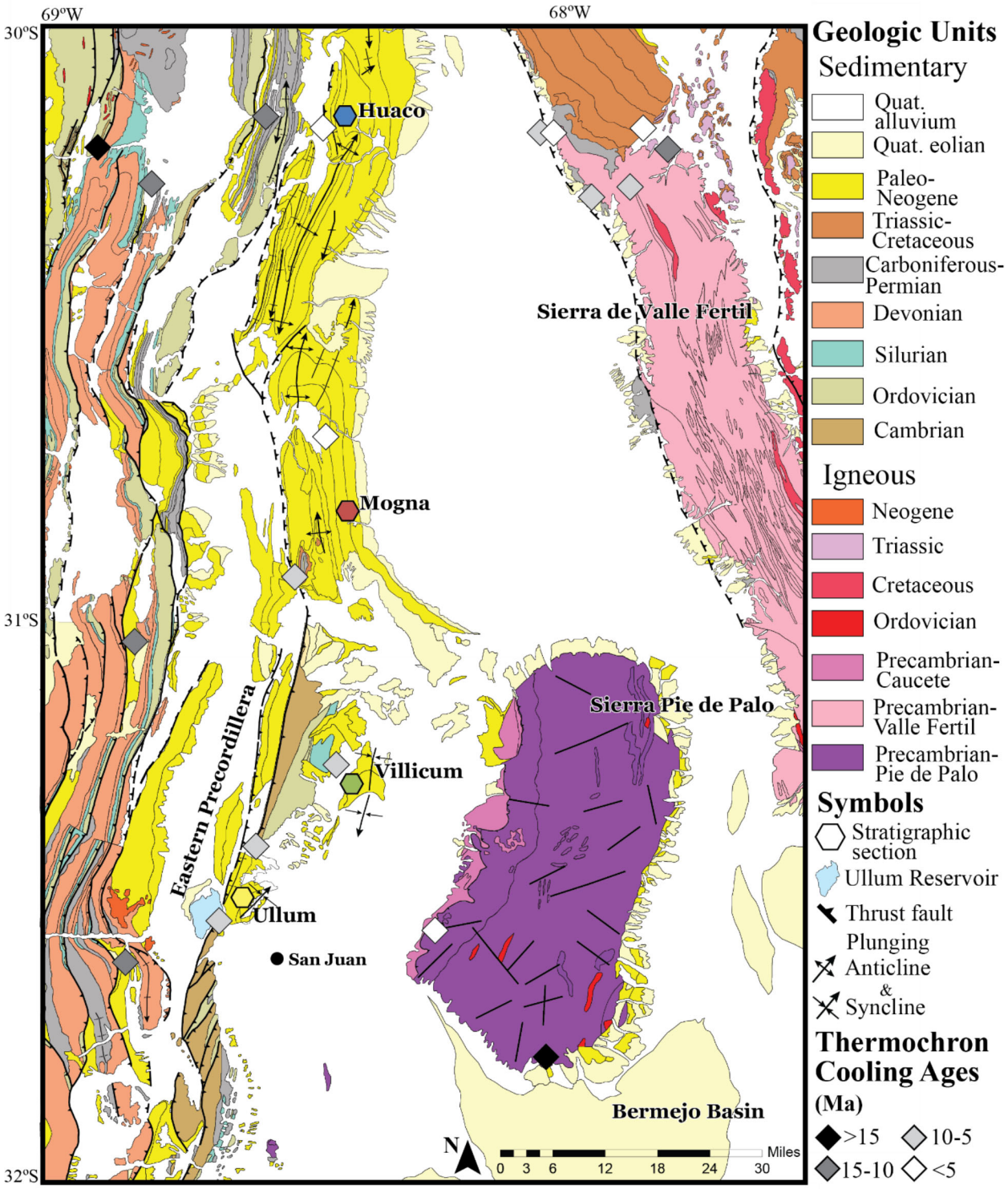

Figure 2: Geologic map of the Argentina broken foreland study area (modified from Ramos et al., 2000; Furque et al., 2003). Stratigraphic sections shown in colored hexagons. Published and new low-temperature apatite (U-Th)/He cooling ages shown in colored diamonds (Lobens et al., 2013; Levina et al., 2014; Fosdick et al., 2015; Ortiz et al., 2015; 2021)

3. SEDIMENTOLOGY

Two new stratigraphic sections in southern Bermejo (Villicum and Ullum) are the focus of this study, with an emphasis on correlation to northern Bermejo sections with existing published datasets (Fig. 3). New sedimentological constraints from the Villicum and Ullum depocenters are expected to reveal changes in foreland depositional environments, sediment provenance, and accumulation rates as the retroarc region was structurally partitioned by Andean ranges. Southern Bermejo stratigraphic sections consist of the Miocene Lomas de las Tapias Formation comprised of the Limolita la Colmena and Arenisca Albardón Members, the Mogna Formation, and the El Corral Formation (Fig. 3; Bercowski, 1987; Contreras et al., 2019). The Limolita la Colmena Member correlates with the upper half of the Quebrada del Jarillal Formation and the Arenisca Albardón Member correlates with the Huachipampa, Quebrada del Cura, and Rio Jachal Formations of northern Bermejo (Fig. 3; after Johnson et al., 1986; Milana et al., 2003).

To assess depositional processes and environments, lithological descriptions, bed thicknesses, facies, and sedimentary structures were described at the decimeter scale in the field. Lithofacies are modified after Miall (1978) and are available in Table 1 along with depositional environment interpretations. Paleoflow directions were determined from imbricated conglomerate clasts (n=15) from localities within the Ullum and Villicum sections (Appendix B). Imbricated conglomerate clast measurements were then corrected for bedding dip using the Stereonet 11 program (Allmendinger, 2012). Mean azimuthal vectors were calculated using the GeoRose software and plotted as paleoflow direction at corresponding stratigraphic heights.

Pebble to boulder sized conglomerate clast compositional data were collected from eight locations within the Villicum section and nine locations within the Ullum section (Fig. 4; Table 2

and 3; Appendix A). Clasts were divided into seven categories: (1) felsic volcanic rocks of Permian-Triassic rhyolite suite consisting of maroon, brown, and red andesite, dacite, and rhyolite volcanic rocks and gray volcaniclastics; (2) felsic intrusive rocks consisting of granitic to granodiorite compositions; (3) mafic to intermediate volcanics consisting of green to gray andesites, and black phenocrystic basalts; (4) meta-sedimentary rocks consisting of green to tan metamorphosed sandstone and siltstone from Silurian-Devonian strata; (5) brown, gray, and red silt- and sandstones; (6) metamorphic lithologies including amphibolite gneiss, schist, marble, and vein quartz from Precambrian-Ordovician basement; and (7) black chert, blue-gray limestone, and dolomite that are derived from Paleozoic carbonates, which are only observed at the base of the Villicum section.

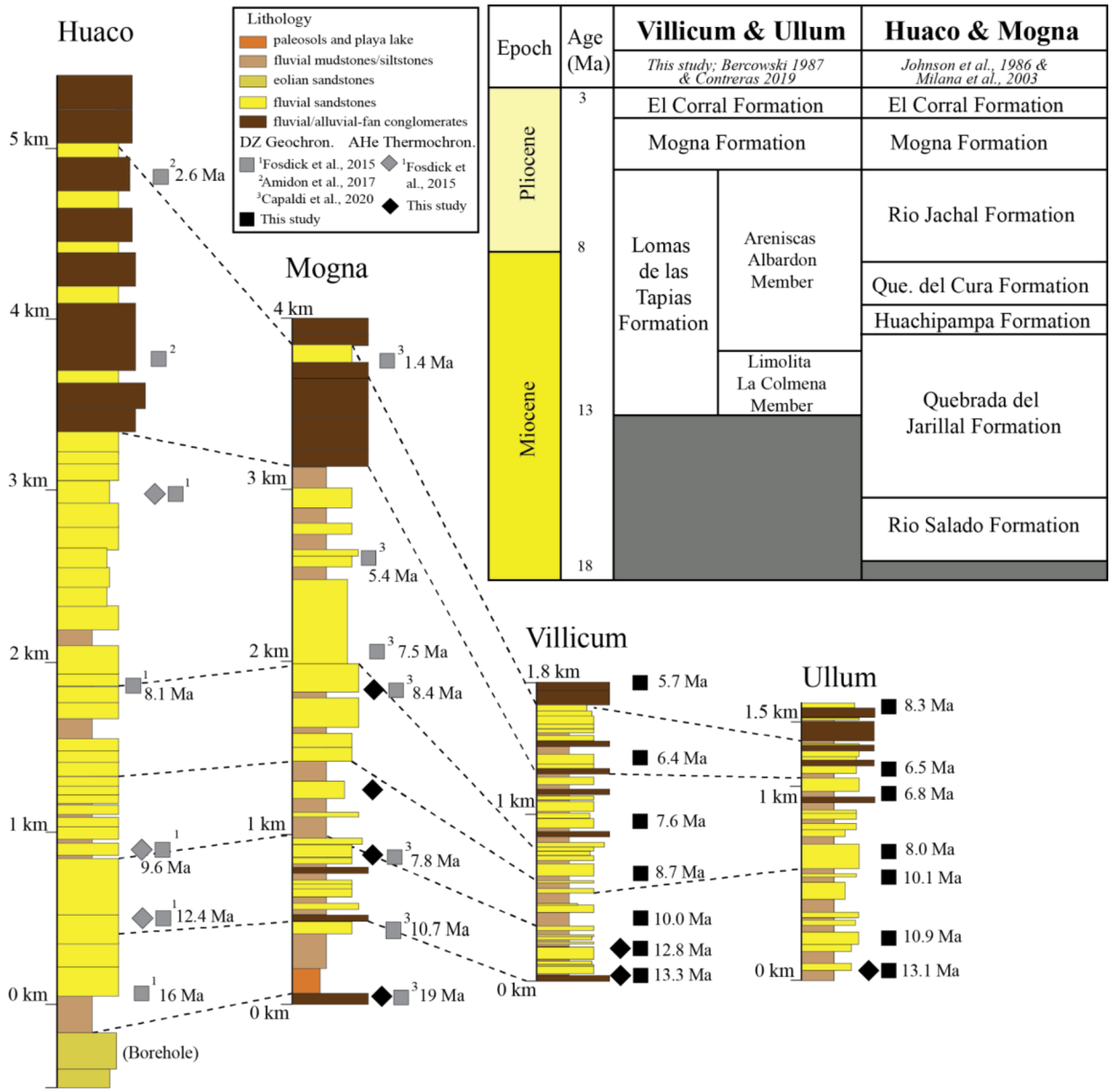

Figure 3: Schematic stratigraphic sections, facies, location of geo-thermochronology rock samples with associated maximum depositional ages, and correlated formations across the Argentina retroarc broken foreland basin system.

3.1. Miocene Lomas de las Tapias Formation: Limolita la Colmena Member

The approximately 325-meter-thick Limolita la Colmena Member of the Lomas de las Tapias Formation sits unconformably on the Cambrian La Lajas Formation at Ullum and the Silurian El Rinconada Formation at Villicum (Fig. 2). Limolita la Colmena largely consists of <5 to ~20 meters of thickly-bedded mud- to siltstones (*Fr;* Facies 1) and thin <1 meter up to ~5 meters thick interbedded very fine to medium grained sandstones (*Fl;* Facies 2) that are more commonly found near the top of the member. There are several occurrences of ~1-meter-thick granule-pebble conglomerate units within the member which provide opportunity for paleoflow and conglomerate clast measurements. The Limolita la Colmena Member is generally an upward-coarsening sequence with facies becoming both sandier/coarser and thicker up-section. Within the Limolita la Colmena Member, abundant gypsum and carbonate nodules *(P)*, on the scale of <5 cm are observed within the mud-siltstone units. At the Villicum section, gypsum is also present in vast vein networks (~1-5 cm) spanning entire mudstone beds of ~3-5 meters in thickness (Fig. 5a). The member is heavily mottled, displaying irregular coloration with frequent occurrences of bioturbation and root structures throughout, and minor occurrences of desiccation structures (*Fr, Fm*; Fig. 5b and 5c). In Villicum, the Limolita la Colmena member also displays mud rip-up clasts, which was not noted at Ullum. Sandstones within the member display minor ripple structures and fine (cm-scale) planar lamination (*Fl*).

Paleocurrent data collected on imbricated clasts in the Limolita la Colmena Member show a south-southeast trend from measurements collected in Ullum and a southeast trend from Villicum (Fig. 4). Conglomerate clast composition of the Limolita la Colmena Member in the Ullum section is dominated by felsic volcanic rocks (47%), metasedimentary rocks (27%), and mafic volcanics (19%). The remaining 9% of clasts consist of minor portions of felsic intrusives and crystalline

basement rock lithologies. In the Villicum section, the base of the Limolita la Colmena member shows local input of underlying Paleozoic carbonate lithologies, representing 81% of clast composition. The remaining 19% consists of metasedimentary clasts. In the upper-section of the member, the Villicum section displays similar trends to Ullum with the dominating lithologies being: felsic volcanics (50%), mafic volcanics (~30%), and metasedimentary rocks (~15%).

The Limolita la Colmena Member has previously been interpreted to represent a playa lake depositional environment (Bercowski et al., 1987; Contreras et al., 2019). The observed upward coarsening sequence, with massive reddish muds that grade into thicker sand channels could further indicate a flood-plain environment (Limarino et al., 2001). Additionally, there are distinct fluvial signals within the Limolita la Colmena Member, represented by the upward thickening packages of laterally continuous sandstones which may indicate unconfined flow in a floodplain, e.g. crevasse splay facies (Horton and DeCelles, 2001). The observed stratigraphic trend of playa lake/paleosol mud-siltstones overlain by fluvial sandstone channels may suggest avulsion of channels within this distal floodplain environment (DeCelles et al., 1998; Horton and DeCelles, 2001). The presence of playa lake-floodplain facies with a distinct fluvial signature may be indicative of a developing fluvial megafan sequence in which the Limolita la Colmena member represents the furthest reaches of an eastward migrating system (e.g. Horton and DeCelles, 2001; Lawton et al., 2014).

3.2. Miocene Lomas de las Tapias Formation: Arenisca Albardón Member

Arenisca Albardón is the uppermost member of the Lomas las Tapias Formation, conformably overlies the Limolita de la Colmena Member, and is ~775 and ~1050 meters thick at Ullum and Villicum, respectively. Arenisca Albardón contains packages of bioturbated and occasionally desiccated mud-siltstones (*Fr, Fm;* Fig. 5c) overlain by laminated and minorly

rippled fine to coarse grained sandstones (*Fl*). Mud-siltstones rarely contain gypsum/carbonate nodules as seen in the Limolita la Colmena Member. Recurring mudstone-sandstone sequences range from 0.25 to 5 meters thick (facies 3). Also significant in the Arenisca Albardón Member are frequent very fine to very coarse sand bodies which display trough and planar cross bedding *(St, Sp;* Fig. 5g) and planar laminae (*Fl*) (facies 4). These sand bodies typically outcrop as multi-story sandstone beds and display flat channel bottoms that are laterally continuous. Granule to pebble clasts are locally present within sandstone beds as floating clasts and occasionally define cross-strata structures (Fig. 5g). Within this sequence there is a notable increase in granule-pebble conglomerate beds which display planar-trough cross stratification and imbricated clasts *(Gp, Gt, Gh)*. Conglomerate beds are typically interbedded within the sandstone bodies of facies 4 or within upward fining sequences where thin conglomerate beds are overlain by the sandstone and siltstone units of facies 3 (<5-meter packages). The Arenisca Albardón Member is composed of repeated fining upward sequences of finer-grained mud-silt-sandstone packages (facies 3) and laterally continuous cross-bedded sand bodies with interbedded conglomerate beds (facies 4) on scales ranging from 5 up to 50 meters (Figs. 5d and 5h).

Paleocurrent measurements from imbricated conglomerate clasts in the Arenisca Albardón Member record south-southeast paleoflow from Ullum sites and eastward paleoflow from Villicum sites (Fig. 4). Conglomerate clast compositions in the Ullum section record a notable decrease in the input of felsic volcanics from 45% at the base to 36% at the top of the member. The percent composition of metasedimentary clasts increase up-section, reaching a maximum of 53% at 525 meters and then steadily declining to 32% at the end of Arenisca Albardón deposition. Mafic volcanics drop to a minimum of 8% coeval with maximum metasedimentary input, and then stabilize around 16% near the top of the member. Within the Villicum section, felsic volcanic

compositions initially increase from 52% to 63% at the base of the member and then decrease to 48% at the top. At this time, metasedimentary clasts steadily increase to 46%, becoming more dominant than mafic volcanics, which decrease to <5% at the end of Arenisca Albardón deposition. Both section locations display low abundances (<10%) of felsic intrusive, brown-red-tan silt-sandstones, and basement rock clasts.

The Arenisca Albardón Member represents an increasingly fluvial environment where the dominant thick, cross-bedded sandstones signify deposition in broad braided river channels and the bioturbated, mottled mud-silt-sandstones represent overbank deposition of finer grained sediment (Miall, 1977; Ciccioli et al., 2018). The laterally continuous flat channel bottoms noted consistently in the multi-story sandstone beds (facies 4) imply no significant incision into adjacent floodplain deposits, indicative of channel avulsion rather than migration (Horton and DeCelles, 2001). Further, the preservation of thick sandy (flat-bottomed) channels interbedded with overbank facies consistently repeated throughout the Arenisca Albardón Member suggests a lack of channel stability over time and is typical of ancient fluvial megafan sequences (Horton & DeCelles 2001).

3.3. Pliocene Mogna Formation

The Pliocene Mogna Formation conformably overlies the Lomas de las Tapias Formation and is ~300 to 325 meters thick in southern Bermejo depocenters. The Mogna Formation largely consists of pebble to cobble conglomerates (facies 5) that are moderately-sorted, contain fair to well-rounded clasts and are typically clast-supported (*Gh*). Conglomerate beds also contain imbricated clasts and planar-cross beds (*Gp, Gh*; Fig. 5f). Thin beds of siltstone to very coarse sandstones typically overly the more abundant conglomerate facies and define upward fining sequences ranging from 2 to 20 meters thick (Fig. 5i). Siltstones display minor bioturbation (*Fr*) and sandstone beds show minor trough-cross to inclined bedding and occasionally preserve meter

scale scour and fill structures infilled by conglomerates (*Ss, Sl*). Sandstone-pebble conglomerate channel bodies most commonly preserve planar bases.

Paleoflow data from the Mogna Formation collected on imbricated conglomerate clasts from southern Bermejo depocenters records south-southeast to southeast sediment dispersal. Within the Mogna Formation at Ullum, felsic volcanic rocks remain a steady contributor of conglomerate clasts at ~35% and mafic volcanic clasts reach a maximum in the upper Mogna Formation at 22%. Metasedimentary clast input increases slightly to 37%, while brown-red-gray silt-sandstones decrease from their maximum at the end of Arenisca Albardón deposition to 4%. In the Villicum section, felsic and mafic volcanics increase slightly, to 53% and 10% respectively. Metasedimentary contribution decreases to 30% and the remaining categories (felsic intrusives and basement lithologies) remain at <10% composition.

The Mogna Formation is interpreted to represent a gravel-dominated braided fluvial environment based on observations of internally upward fining cycles of conglomerate and coarse sandstone capped by silty mudstones (Miall, 1977, 1985; Ciccioli et al., 2018; Capaldi et al., 2020). This broad braided river is interpreted to represent the main channel of the fluvial megafan system that is continuing to migrate eastward at this time due to deformation in the hinterland, based on observations of planar channel bases and continuation of overbank facies preservation (Horton and DeCelles, 2001). Up-ward coarsening successions, as seen in both Villicum and Ullum, where ephemeral lake systems grade into sandy to coarse conglomerate avulsing channel deposits with interbedded overbank/crevasse splay facies, record progradation of a fluvial megafan as the adjacent fold-thrust belt (Precordillera) advances eastward (Horton and DeCelles, 2001; Lawton et al., 2014).

3.4. Pliocene El Corral Formation

The Pliocene El Corral Formation rests conformably on the Mogna Formation and was locally measured to 60 and 125 meters thick at Villicum and Ullum, respectively. Based on estimated true thickness of the southern Bermejo sections, the El Corral Formation may have an actual thickness up to 300 meters (see section 2). The El Corral Formation is dominated by pebble to cobble conglomerate lithofacies with occasional floating boulder-sized clasts (*Gcm)*, and is matrix to clast supported, poorly sorted and structureless (*Gcm;* Fig. 5e*)*. The conglomerate units are interbedded with thin (0.5 to <5 m) beds of siltstone (near the base) and medium to coarse grained sandstone (up-section; *Fl-Sm*), defining upward fining packages from 5 to 20 meters thick.

Paleocurrent data collected on imbricated clasts at both southern Bermejo depocenters from the El Corral Formation produce east-southeast to southeast paleoflows. Conglomerates of the El Corral Formation in Ullum are dominated by metasediments (48%). Felsic volcanic rock input remains steady at ~30% and mafic volcanic clasts decreased slightly to their average around 16%. Felsic intrusive rocks, brown-grey-red silt-sandstones, and basement rocks individually contribute <5%. In Villicum, the El Corral Formation is similar to that of Ullum with 42% felsic volcanic input and 40% metasedimentary rock input. Felsic intrusives reach a maximum at this point of 10% while mafic volcanics remain steady around ~8%.

The poorly sorted, structureless pebble-cobble conglomerate facies of the El Corral Formation are interpreted as gravelly debris flows and late-stage sandy hyperconcentrated flow on an alluvial fan (Nemec & Steel, 1984; Horton & Schmitt, 1996; Perez & Horton, 2014). The El Corral debris flow deposits are interbedded with fluvial silt-sandstone units (braided river channels seen in the Arenisca Albardón Member) and are likely signaling the increase in energy associated with the approaching topography of the Precordillera thrust-front towards the foreland.

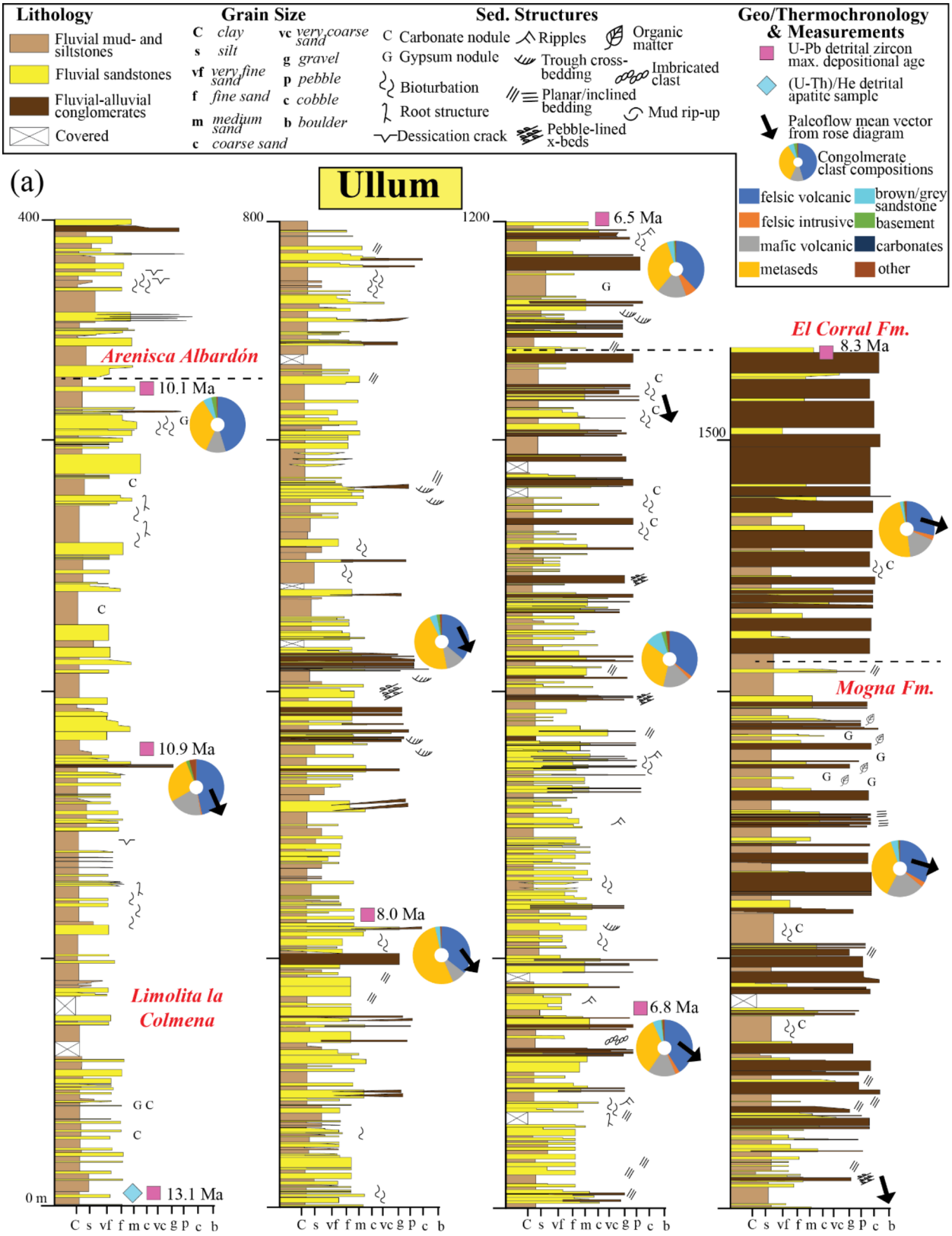

Figure 4: Stratigraphic sections from southern Bermejo basin. Sections show location of rock samples and associated depositional age, paleocurrent measurements (arrows), clast count compositions (donut diagrams), and observed sedimentary structures (a) Southern Bermejo basin, Ullum section. Cont.

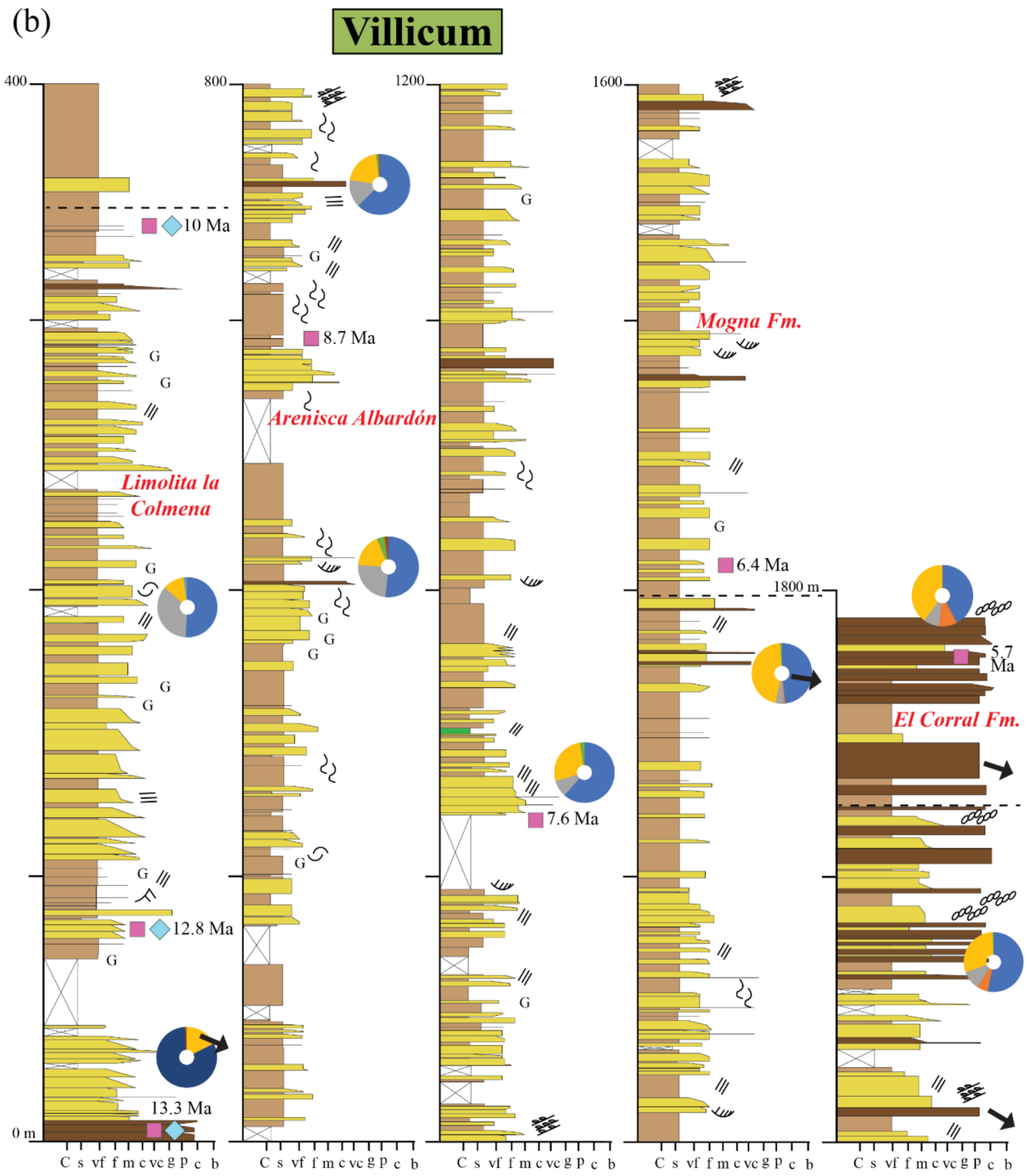

Figure 5: (b) Southern Bermejo basin, Villicum section.

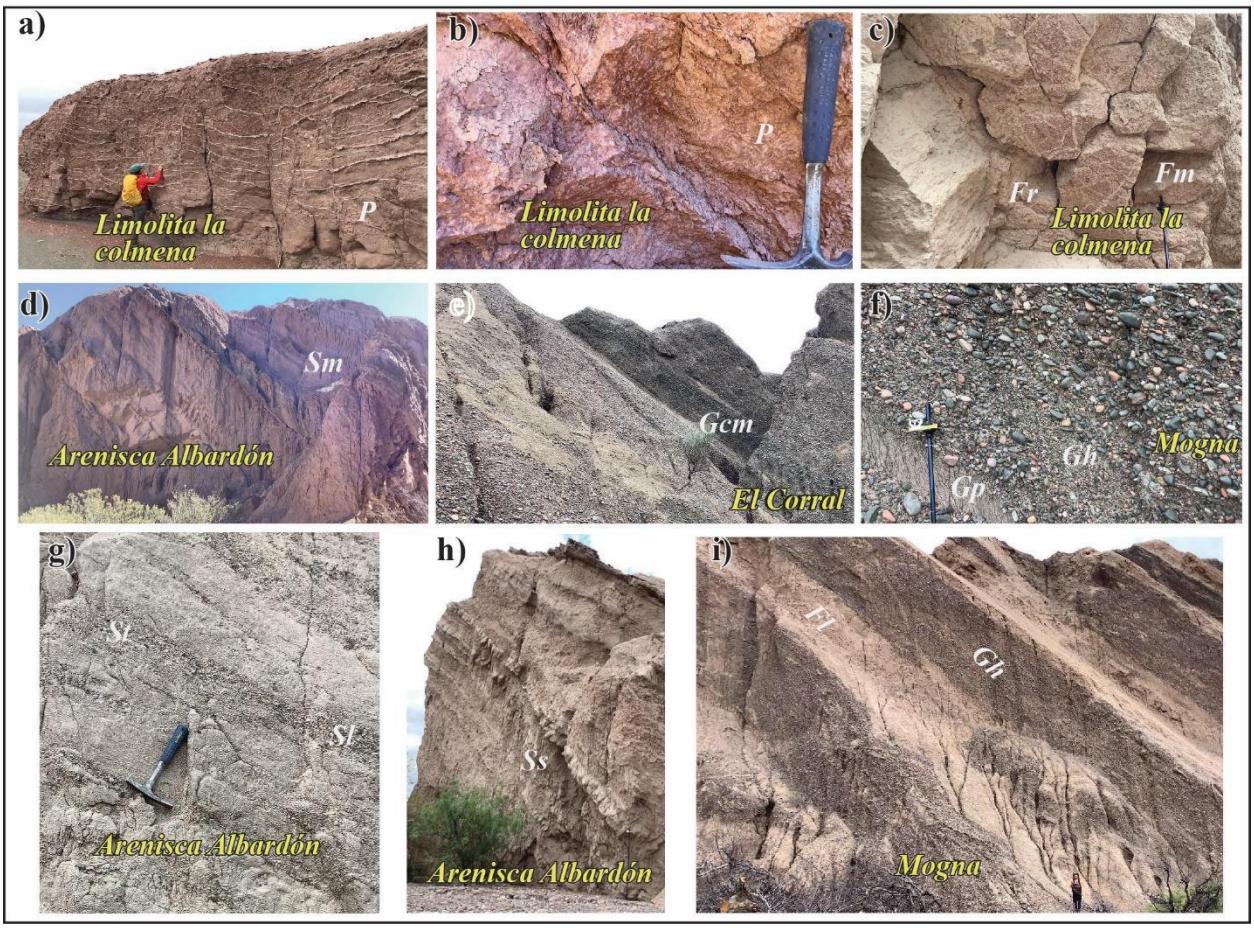

Figure 6: Field photographs of sedimentary deposits of the Villicum and Ullum sections. (a) Gypsum veins (P) in the Limolita la Colmena Member at Villicum. (b) Limolita la Colmena paleosol facies at Ullum (P); mottled mud-siltstone displaying discoloration and bioturbation. (c) Desiccation structures preserved in mud-siltstone (Fm) with roots and bioturbation (Fr) in Limolita la Colmena at Ullum. (d) Large-scale packages of laterally continuous, flat bottomed sandstone beds (Sm) diagnostic of the Arenisca Albardon Member at Ullum (30-50-meter packages). (e) Poorly sorted, structureless cobble-dominated conglomerate (Gcm) of the El Corral Formation at Ullum. (f) Imbricated and slightly cross-bedded pebble conglomerates (Gp, Gh) of the Mogna Formation at Ullum. (g) Cross-bedded sandstone (St, Sl) of the Arenisca Albardon Member at Ullum incorporating coarser-grained sediment, at Ullum. (h) Crevasse splay facies of the Arenisca Albardon Member at Ullum (~5-10-meter packages). (i) Interbedded pebble-cobble conglomerates (Gh) and silt-sandstone (Fl) of the Mogna Formation at Ullum.

Table 1

Facies and interpretations for southern Bermejo basin deposits

Facies	Lithofacies	Description	Occurrence	Interpretation
1	Fr, P	Massive reddish mud-siltstones. Mottled, bioturbated, common carbonate and gypsum nodules/veining.	Limolita la Colmena Mb.	Playa lake, paleosol
2	Fl, Fr, Fm, Gp	Massive red-tan mud-siltstones grade into very fine to medium grained, laterally continuous and minorly rippled sandstones. Mud-silts are bioturbated and desiccated.	Limolita la Colmena Mb.	Floodplain
3	Fr, Fm Fl	Bioturbated and ocasionally desiccated mud-siltstones overlain by laminated, minorly rippled fine-coarse sandstone.	Arenisca Albardón Mb., Mogna Fm.	Fluvial overbank with crevasse-splays
4	Fl, St, Sp Gp, Gh Gt	Very fine-very coarse cross bedded and laminated sandstones. Laterally continuous with flat channel bottoms.Cross bedded and imbricated granule- pebble conglomerates.	Arenisca Albardón Mb., El Corral Fm.	Sandy fluvial channels in a distal megafan
5	Gh, Gp, Fr Ss, Sl	Granule-cobble coglomerates that are moderately sorted, fair-well rounded, and clast supported. Fines upwards into silt-sandstones. Preserved flat channel bottoms.	Mogna Fm.	Main fluvial megafan channel
6	Gcm, Fl Sm	Pebble-cobble conglomerate with occasional floating boulder clast. Matrix-clast supported, poorly sorted, and structureless.	El Corral Fm.	Debris flow

Table 1: Facies and interpretations for southern Bermejo basin deposits.

	CC01		CC02		CC03		CC04		CC05		CC06		CC07		CC08		CC09	
Clast Categories	n	%	n	%	n	%	n	%	n	%	n	%	n	%	n	%	n	%
(1) Felsic Volcanic	70	47	63	45	49	36	59	36	67	41	53	36	58	38	57	33	42	29
(2) Felsic intrusive	1	1	0	0	0	0	0	0	4	2	3	2	10	6	5	3	4	3
(3) Mafic volcanic	29	19	16	12	11	8	18	11	26	16	24	16	26	17	37	22	24	16
(4) Metaseds	41	27	48	35	73	53	75	46	55	34	47	32	52	34	64	37	70	48
(5) Brown/Grey SS	0	0	7	5	4	3	7	4	8	5	15	10	6	4	7	4	3	2
(6) Basement	3	2	4	3	0	0	3	2	1	1	4	3	1	1	1	1	1	1
(7) Carbonates	0	0	0	0	0	0	0	0	0	0	0	0	0	0	0	0	0	0
(8) other	6	4	1	1	1	1	2	1	2	1	3	2	1	1	1	1	2	1
Total	150	100	139	100	138	100	164	100	163	100	149	100	154	100	172	100	146	100

Table 2: Clast compositional data for the Ullum section using categories described in section three. Highlighted columns show representative percentages used to calculate donut diagrams in figure 4a.

	CC01		CC02		CC03		CC04		CC05		CC06		CC07		CC08	
Clast Categories	n	%	n	%	n	%	n	%	n	%	n	%	n	%	n	%
(1) Felsic Volcanic	0	0	183	51	75	52	94	63	75	61	55	48	89	53	57	42
(2) Felsic intrusive	0	0	0	0	0	0	0	0	0	0	1	1	10	6	13	10
(3) Mafic volcanic	0	0	127	35	35	24	22	15	11	9	5	4	17	10	11	8
(4) Metaseds	35	18	42	12	26	18	31	21	33	27	52	46	50	30	54	40
(5) Brown/Grey SS	0	0	6	2	0	0	0	0	0	0	0	0	0	0	0	0
(6) Basement	0	0	0	0	6	4	2	1	3	2	1	1	1	1	0	0
(7) Carbonates	162	81	0	0	0	0	0	0	0	0	0	0	0	0	0	0
(8) other	2	1	1	0	3	2	1	1	0	0	0	0	0	0	0	0
	199	100	359	100	145	100	150	100	122	100	114	100	167	100	135	100

Table 3: Clast compositional data for the Villicum section using categories described in section three. Highlighted columns show representative percentages used to calculate donut diagrams in figure 4b.

4. DETRITAL ZIRCON U-PB GEOCHRONOLOGY

We collected 14 sandstone samples within the measured stratigraphic sections (Fig.4) and an additional 2 sandstone samples (ULL01 and VIL01) not in the stratigraphic sections (Fig. 2; Appendix E). We targeted medium-grained sandstones for zircon U-Pb geochronology to determine maximum depositional ages of Neogene units, and to constrain changes in sediment provenance during uplift and erosion of Andean ranges. Zircon is a highly refractory mineral that incorporates high concentrations of U combined with low amounts of initial Pb providing precise age controls for the crystallization of intermediate to felsic igneous rocks and high- grade metamorphic rocks (Gehrels, 2014; Rubatto, 2017).

4.1. Methodology

Zircons were extracted from sandstones using standard separation procedures including crushing, grinding, water table, heavy liquid density, and magnetic susceptibility. Zircon grains were handpicked using an optical microscope, targeting non-broken, inclusion-free grains, and were mounted on double sided tape on 2.5 cm diameter epoxy resin mounts. Zircon grains were chosen randomly for analysis by laser-ablation-inductively coupled plasma-mass spectrometry (LA-ICP-MS) to obtain zircon U-Pb ages.

At the University of Texas at Austin UTChron laboratory sample mounts were loaded into a large-volume Helex sample cell and ablated using a PhotonMachine Analyte G.2 excimer laser for analysis with a single-collector, magnetic sector Element2 ICP-MS (Capaldi et al., 2021). Corrections for depth dependent, elemental and isotopic fractionation were performed using zircon standard GJ1 (600.4 ± 0.1 Ma; Jackson et al., 2004). Secondary standards were analyzed

periodically to verify the accuracy of the analyses; these included the Plesovice zircon (PL-1; 337.2 ± 0.4 Ma; Sláma et al., 2008) and Pak-1 (43.03 Ma; in-house standard).

At the Nevada Plasma Facility Lab at the University of Nevada, Las Vegas, sample mounts were loaded into a TwoVol 1 ablation cell and ablated using an ESI 193 nm NWR193 excimer laser for analysis with a Quadruple collector ThermoFisher Scientific TM iCAP ICP-MS (Garzanti et al., 2022). Corrections for depth-dependent, elemental and isotopic fractionation were performed using zircon standards FC1 (1099 ± 0.5 Ma; Paces and Miller, 1993) and secondary standards Plesovice (PL-1; 337.2 ± 0.4 Ma; Sláma et al.,2008) and Fish Canyon Tuff (28.4 ± 0.02 Ma; Schmitz and Bowring, 2001).

Zircon analyses were reduced using the VizualAge™ workflow in the Iolite™ plugin for Igor Pro™ (Paton et al., 2011; Petrus and Kamber, 2012). Zircon U-Pb ages and 2σ errors are reported for analyses with <10% $^{206}Pb/^{238}U$ uncertainties, <20% discordance, and < 5% reverse discordance. Reported values for grains < 1200 Ma are $^{206}Pb/^{238}U$ ages with $^{206}Pb/^{238}U$ vs. $^{207}Pb/^{235}U$ discordance, whereas values for grains > 1200 Ma ages are $^{207}Pb/^{206}Pb$ ages with $^{206}Pb/^{238}U$ vs. $^{207}Pb/^{206}Pb$ discordance. Miocene zircons (<23 Ma) were expanded to incorporate ages with < 20% $^{206}Pb/^{238}U$ uncertainties and < 50% discordance $^{206}Pb/^{238}U$ in order to prevent biasing due to exclusion of young grains with higher ^{207}Pb and associated calculated $^{207}Pb/^{235}U$ ages that are systematically older than measured $^{206}Pb/^{238}U$ ages (Appendix E).

Results for individual samples are arranged in stratigraphic order and are represented as kernel density estimations (KDEs; with a set bandwidth of 20 M.y.) with histogram age bins (Figs. 6, 7, 8) and plotted using IsoplotR (Vermeesch, 2018). Comparison among sandstone samples U-Pb age distributions was accomplished by visual inspection of the relative abundance of age

groups. Additional DZ U-Pb age distributions comparison was established through metric multidimensional scaling (MDS) plots to identify greater similarity for samples that cluster together and less similar for those that plot farther apart. Metric squared MDS is applied by constructing a pairwise dissimilarity matrix of detrital age distributions among the sandstone samples using R^2 cross-correlation coefficient. Metric squared MDS plot and results were created using the program DZmds (Saylor et al., 2018). Detrital zircon samples from the Andean foreland deposits from the Ullum and Villicum sections were compared to each other and to previously published data from Huaco section (Fosdick et al., 2015; Amidon et al., 2017) and Mogna section (Capaldi et al., 2020) using a three-dimensional (3D) MDS plot. The misfit from conversion of sample dissimilarity to disparity in Cartesian space via linear transformation gives a good correlation as indicated by a low stress minimum (0.08).

4.2. Maximum Depositional Ages

A maximum depositional age for the 16 sandstone samples was derived from the calculated weighted mean age of the youngest grain cluster overlapping by 2σ concordant U-Pb ages (following approaches established by Dickinson and Gehrels, 2009; Coutts et al., 2019). In cases where two or more grains do not overlap by 2σ, the youngest single grain was selected as the maximum depositional age (Tables 4 and 5; Appendix C) and plotted at the corresponding stratigraphic level (Fig. 4).

Most Cenozoic sandstone samples contain young age populations broadly consistent with previous age assessments (Milana et al., 2003; Capaldi et al., 2020). Collectively, samples from the retroarc basin system show a systematic up-section decrease in maximum depositional age, with the exception of sample ULL08 (8.3± 0.1 Ma) from El Corral Formation in the Ullum section

(Fig. 4). On the basis of the internal consistency and stratigraphic coherence, the calculated maximum depositional ages are regarded as viable approximations of stratigraphic age.

4.3. Detrital Zircon Age Components

Here we describe five diagnostic age groups representative of sediment provenance signatures recorded by detrital zircon U-Pb analyses from oldest to youngest:

1. Proterozoic zircon ages (~925-1450 Ma) ages include a 1350-1450 Ma age component recycled from Cambrian-Ordovician strata unique to the Laurentian-derived Cuyania terrane presently exposed along the Eastern Precordillera (Ramos et al., 1986; Thomas et al., 2015; Martin et al., 2019). Dominant 925-1200 Ma zircon age components are sourced from numerous Sunsas metamorphic basement units that outcrop presently across the western Sierras Pampeanas and are ubiquitous in most Ordovician to Permian sedimentary sequences deformed within the central Precordillera (Ramos, 2004, 2009; Bahlburg et al., 2009; Rapela et al., 2016).

2. The Eastern Sierras Pampeanas (515-725 Ma) age group is composed of a minor 725-550 Ma age component initially recycled from sourced metasedimentary rocks (Puncoviscana Formation) and a dominant Ediacaran-Cambrian 515-550 Ma age peak originally from evolved igneous-metamorphic rocks of the Pampean magmatic arc presently found in Sierra Cordoba (Schwartz et al., 2008; Rapela et al., 2016). The Eastern Sierras Pampeanas (515-725 Ma) age group zircons are commonly recycled from Carboniferous to Permian sedimentary sequences found in the central Precordillera fold-thrust belt (Fosdick et al., 2015; Capaldi et al., 2017; 2020).

3. The Western Sierras Pampeanas (380-510 Ma) age group is derived from sources throughout the western Sierras Pampeanas involving 440-505 Ma Famatinian continental arc rocks (Ducea et al., 2010; Otamendi et al., 2017; Rapela et al., 2018) and subsequent 385-435 Ma aged metamorphic assemblages associated with accretion of the Cuyania terrane (Coira et al., 1982;

Astini et al., 1995; Martin et al., 2019). Recycled western Sierras Pampeanas 380-510 Ma DZ age components are derived from Carboniferous-Permian sedimentary units in the Precordillera fold-thrust belt and Carboniferous-Triassic sedimentary sequences overlying western Sierras Pampeanas uplifts (Capaldi et al., 2017).

4. Late Carboniferous-Triassic zircon ages (225-330 Ma) are derived from intrusive and volcanic rock sources throughout the Chilean Coastal Cordillera, Frontal Cordillera, and Principal Cordillera. These rocks include the 290-310 Ma Elqui-Limari and the Colanguil batholiths (Maksaev et al., 2014; Herve et al., 2014; del Rey et al., 2016), and 240-280 Ma granitoids and silicic volcanics of the Choiyoi igneous province (Mpodozis and Kay, 1992; Kleiman and Japas, 2009; Sato et al., 2015).

5. East-dipping subduction generated the Jurassic to Cenozoic Andean magmatic arc (0-200 Ma), which is defined by north-trending belts involving principally granite/granodiorite intrusions and andesite flows. These belts show a systematic eastward decrease in age, from Jurassic (200–165 Ma) and Cretaceous (130–90 Ma) rocks along the Chilean coast, to Paleocene– Eocene (67–38 Ma) and Eocene– Oligocene (27–18 Ma) units along the western flank of the Principal Cordillera, and finally Miocene (17–4 Ma) volcanic rocks in the eastern Principal Cordillera, Frontal Cordillera, and Argentine foreland (Kay et al., 1991; Haschke et al., 2006; Jones et al., 2016; Capaldi et al., 2021).

4.4. Detrital Zircon Age Results

Detrital zircon U-Pb age distributions from 14 sandstone samples from the Villicum and Ullum stratigraphic sections indicate ~7 million years of deposition and are plotted based on depositional age from old to young (bottom to top; Fig. 6). Distinctive age signatures from the five

diagnostic age groups are highlighted in color bars and relative percent contributions are plotted as ring diagrams (Fig. 6), and a summary of results will be discussed in the following paragraphs.

Samples from the Villicum stratigraphic section display an overall upsection increase in both Western and Eastern Sierras Pampeanas (early Paleozoic arcs) and Proterozoic basement age components during deposition from 13.3 to 5.7 Ma. All of the Villicum samples contain a significant amount of Andean Arc age grains ranging from 23-60%. Andean Arc age components show an initial decrease from 60% to 33% between 13.3 and 10 Ma. Andean Arc grains then increase and peak at 54% in the 7.6 Ma aged sample (VILE09), and then begin to decrease, reaching a minimum input of 23% at the top of the Villicum section (VILE11). Late Carboniferous to Triassic zircon age components are prevalent from 12.8-5.7 Ma, displaying two notable pulses around 10 Ma (~40%) and 6.4 Ma (~20%). Western Sierras Pampeanas age components represent minor contributions throughout deposition of Villicum, showing an overall upward trend from <1% at the base of the section (VILE04) to ~9% at the end of deposition (VILE11). Eastern Sierras Pampeanas zircon inputs follow roughly the same trend as those of the Western Sierras Pampeanas, increasing from 0% at the start of deposition to a maximum of 18% at the top of the section. Proterozoic basement age components represent 28% of zircon composition at the base of the section in the 13.3 Ma aged sample, then show an initial decrease- reaching a minimum of 8% in the 8.7 Ma aged sample (VILE08). Proterozoic inputs then steadily increase and represent 24% of detrital zircon composition at the top of the section (VILE11).

Detrital zircon age distributions in the Ullum stratigraphic section reveal similar trends to those of Villicum, but evidently have a more complex history in terms of provenance signatures. Contribution of Andean Arc age components are notable in every sample, ranging from 14% to 44%, with no observable pattern in terms of Andean Arc input throughout the duration of

deposition. Late Carboniferous-Triassic aged grains represent a more consistent and dominant source of zircon grains for the Ullum section. There are two notable increases in Late Carboniferous-Triassic age components observed in the 10.1 Ma sample (ULL04) with 55% and at the top of the section (<6.5 Ma; ULL08) with 32%. These increases in Carboniferous-Triassic age components are also observed in coeval deposits in the Villicum section (Fig. 6). Western Sierras Pampeanas age components display an up-section decrease in relative contribution, from 29% in the 13.1 Ma aged sample (ULL02) to 7% in the two uppermost samples of the section (ULL07 & ULL08). Eastern Sierras Pampeanas aged zircon contributions are <10% in 4 lowest samples (ULL02-ULL05) and reach a maximum of 16% in the 6.8 Ma aged sample (ULL06), and then decrease to 10% at the top of the stratigraphic section.

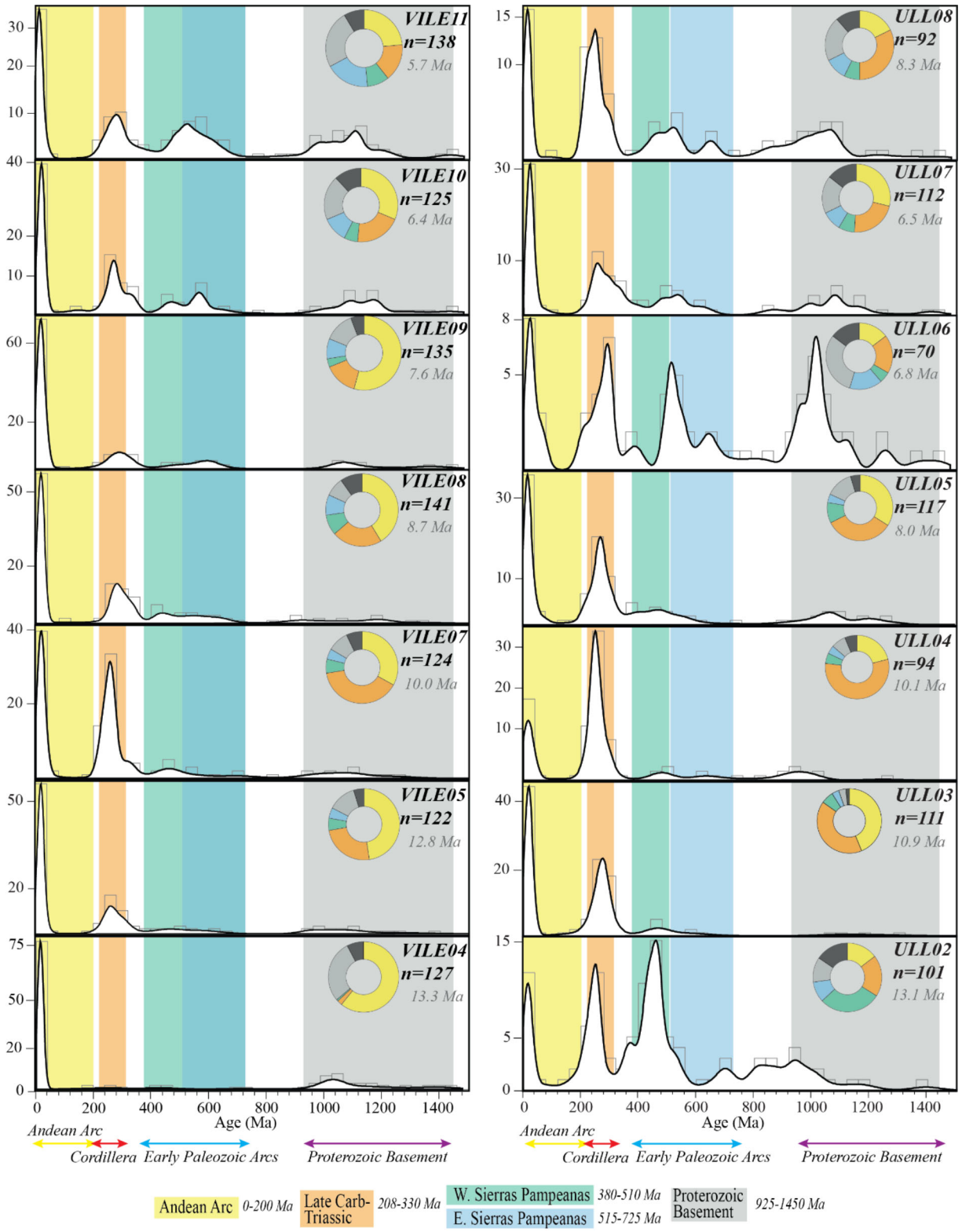

Figure 7: Comparative plot of detrital zircon U-Pb age distributions for sandstone samples. Distributions depicted as kernel density estimates (20 Myr bandwidth) and age histograms with emphasis on key age components (color shading). Ring diagrams at right present the relative abundance of key age components (color shading).

Maximum Depositional Age Calculations			
	Youngest grain cluster at 2σ (YGC 2σ)		
sample	age	error	% disc
ULL02	12.7	1.4	0.3
	13.0	1.1	12.4
	13.0	1.9	38.6
	13.3	2.5	5.8
	13.4	1.3	13.6
	13.4	1.9	23.5
	13.1	**0.2**	
ULL03	10.5	1.3	44.3
	10.5	0.6	0.4
	10.8	0.7	12.8
	11.2	0.8	3.7
	11.3	0.9	17.0
	10.9	**0.3**	
ULL04	9.0	1.5	38.0
	10.6	1.7	48.1
	10.8	2.0	42.2
	10.1	**0.8**	
ULL05	7.8	0.7	16.0
	7.9	1.3	26.5
	8.0	0.9	39.6
	8.1	1.4	46.8
	8.4	0.9	5.6
	8.0	**0.2**	
ULL06	**6.8**	**0.9**	15.3
ULL07	**6.5**	**0.4**	15.7
ULL08	8.2	1.4	42.5
	8.3	1.4	24.1
	8.3	1.6	34.8
	8.3	**0.0**	

Table 4: Maximum depositional ages for Ullum samples using youngest grain cluster at 2σ. In cases where three or more grains do no overlap we rely on youngest single grain (shown in Appendix C). Stratigraphic height of sample collection show on figure 4a.

Maximum Depositional Age Calculations							
	Youngest grain cluster at 2σ (YGC 2σ)						
sample	age	error	% disc	sample	age	error	% disc
VILE04	12.8	0.8	5.3	VILE09	7.1	0.8	24.5
	13.6	1.7	13.4		7.2	1.0	19.7
	13.6	1.0	18.6		7.4	0.8	44.2
	13.3	0.4			7.5	0.9	14.6
VILE05	12.4	0.8	9.0		7.5	0.8	29.4
	12.4	1.0	1.7		7.6	1.3	16.5
	12.8	0.8	11.2		7.6	0.9	17.4
	12.8	2.5	14.1		7.7	0.9	35.2
	12.8	1.0	8.4		8.0	0.6	3.4
	13.2	0.8	7.4		8.0	1.0	33.9
	13.2	1.5	17.0		8.2	0.8	1.8
	12.8	0.3			7.6	0.3	
VILE07	10.0	0.6	2.6	VILE10	**6.4**	**0.4**	7.7
	10.0	0.5	14.1	VILE11	**5.7**	**0.6**	38.4
	10.0	0.0					
VILE08	8.3	0.8	4.8				
	8.4	0.5	14.7				
	8.7	1.2	0.0				
	8.7	0.8	29.6				
	8.7	0.4	11.8				
	8.8	0.9	7.9				
	8.8	0.4	11.7				
	8.9	0.9	33.5				
	9.0	0.7	13.3				
	8.7	0.2					

Table 5: Maximum depositional ages for Villicum samples using youngest grain cluster at 2σ. In cases where three or more grains do no overlap we rely on youngest single grain (shown in appendix C). Stratigraphic height of sample collection show on figure 4b.

5. APATITE (U-TH)/HE THERMOCHRONOLOGY

We conducted detrital apatite (U-Th)/He thermochronologic analyses (AHe) to track the timing of tectonic and/or erosional exhumation in the Eastern Precordillera. We collected 7 sandstone samples from the Mogna, Villicum, and Ullum stratigraphic sections (Fig. 2). Samples were targeted from basal deposits along each stratigraphic section, which are expected to record the highest degree of thermal resetting due to burial of overlying basin sediment. AHe thermochronometry relies on the temperature-dependent retention and diffusive loss of alpha particles (^{4}He) during the radioactive decay of U, Th, and Sm (Farley, 2002). The AHe system is characterized by its relatively low closure temperature that ranges between ~30-90ºC depending on radiation damage accumulation in the crystal (Shuster et al., 2006; Flowers et al., 2009), corresponding to exhumation from ~1–4 km depth assuming a geothermal gradient of 20–26°C/km in the Sierras Pampeanas continental crust (Sobel and Strecker, 2003; Löbens et al., 2013; Collo et al., 2017). Exhumational cooling is often delayed after tectonic activity, and thermochronometric data cannot directly quantify fault activity/uplift, but if cooling is linked to fault-induced displacement and enhanced erosion, AHe ages may serve as a proxy for deformational timing (Ault et al., 2019; Mackaman-Lofland et al., 2020; 2022).

5.1. Methodology

Standard mineral separation was conducted on seven Miocene sandstone samples from foreland deposits exposed along the Eastern Precordillera, which included crushing, grinding, water table, heavy-liquid density, and magmatic susceptibility separations. Apatite grains were handpicked using an optical microscope, targeting non-broken, inclusion-free grains and were measured to calculate the alpha ejection correction factor (Farley, 2000; Elhers & Farley 2003). Single apatite grains were packed into platinum tubes, heated with a diode laser for 10 minutes at

1070º and repeatedly reheated until the ^{4}He yield dropped to <1% to ensure complete degassing. Extracted gas was spiked with a ^{3}He tracer, cryogenically concentrated and purified, and measured with a noble gas quadrupole mass spectrometer at the University of Texas at Austin UTChron laboratory. Apatite aliquots were dissolved using HNO_3-based solution (diluted and purified MilliQ water to 5% $HNO_{3)}$ spiked with ^{235}U, ^{230}Th, and ^{149}Sm tracer. Apatite U, Th, and Sm parent concentrations were measured by isotope dilution-inductively coupled plasma-mass spectrometry (ID-ICP-MS) analysis with a single-collector, magnetic sector Element2 at the University of Texas at Austin UTChron laboratory. Durango apatite were analyzed as independent unknowns to ensure data quality and age accuracy (Boyce & Hodges, 2005). Based on replicate analysis of the Durango apatite standards, analytical uncertainties for uncorrected AHe ages are estimated at 6% (2σ).

5.2. Detrital Apatite Results

AHe dates were compared against maximum depositional ages generated from detrital zircon U-Pb analysis to ensure that the apatite dates we interpret are younger and therefore reset cooling ages that have reached temperatures greater than AHe closure-temperature of ~70°C. Only dates younger than the maximum depositional age from corresponding samples are considered as fully reset and therefore included in our results discussion (Fig. 7). New AHe analyses of seven sandstone samples from the Mogna, Villicum, and Ullum sections yield mean apatite grain dates between 2.8 and 6.1 Ma. All samples will be discussed in increasing stratigraphic order (bottom to top). Reduced (U-Th[Sm])/He data for all samples analyzed is available in Appendix D.

Four samples were analyzed from the Mogna section that yield mean grain ages between 2.8 ± 0.17 and 9.6 Ma. Basal sample MGN08 from Rio Salado Formation produced two aliquots

younger than the zircon MDA (19 Ma) and reveals significantly dispersed ages of 2.7 ± 0.16 Ma and 16.4 ± 0.99 Ma. Sample MGN10 yielded four AHe aliquots that are younger than zircon MDA (11.2 ± 1.1 Ma) which yielded AHe grain ages between 3.5 ± 0.21 and 7.0 ± 0.42 Ma with a mean of 4.7 ± 0.27 Ma. The sample MGN01 produced one aliquot younger than the MDA (7.3 ± 0.8 Ma) at 2.8 ± 0.17 Ma. Uppermost sample MGN02 had 3 aliquots ages between 2.1 ± 0.12 and 5.0 ± 0.3 Ma with a mean age of 3.1 ± 0.17 Ma, all of which are younger than the zircon MDA of 8.2 ± 0.7 Ma.

Two samples were analyzed from the Villicum section that yield mean grain ages of 5.9 ± 0.33 Ma and 5.5 ± 0.29 Ma. All five aliquots from sample VIL01 show grain ages that range from 2.3 ± 0.14 to 7.9 ± 0.47 Ma, which are younger than the corresponding zircon MDA of 11.9 ± 0.4 Ma. Sample VILE07 produced four out of five grain ages younger than the corresponding zircon MDA of 10.0 ± 0.6 Ma, suggesting the sample was only partially reset. The sample yielded relatively dispersed grain ages between 2.4 ± 0.14 Ma and 9.2 ± 0.55 Ma.

One sample was analyzed from the Ullum section with a mean AHe age of 6.1 ± 0.32 Ma. Five of the six aliquots analyzed for ULL01 were younger than the corresponding zircon MDA of 10.6 ± 0.2 Ma with AHe ages that range from 2.2 ± 0.13 to 8.8 ± 0.53 Ma. The dispersed ages suggest partial resetting of the sample from the base of the thinnest stratigraphic section.

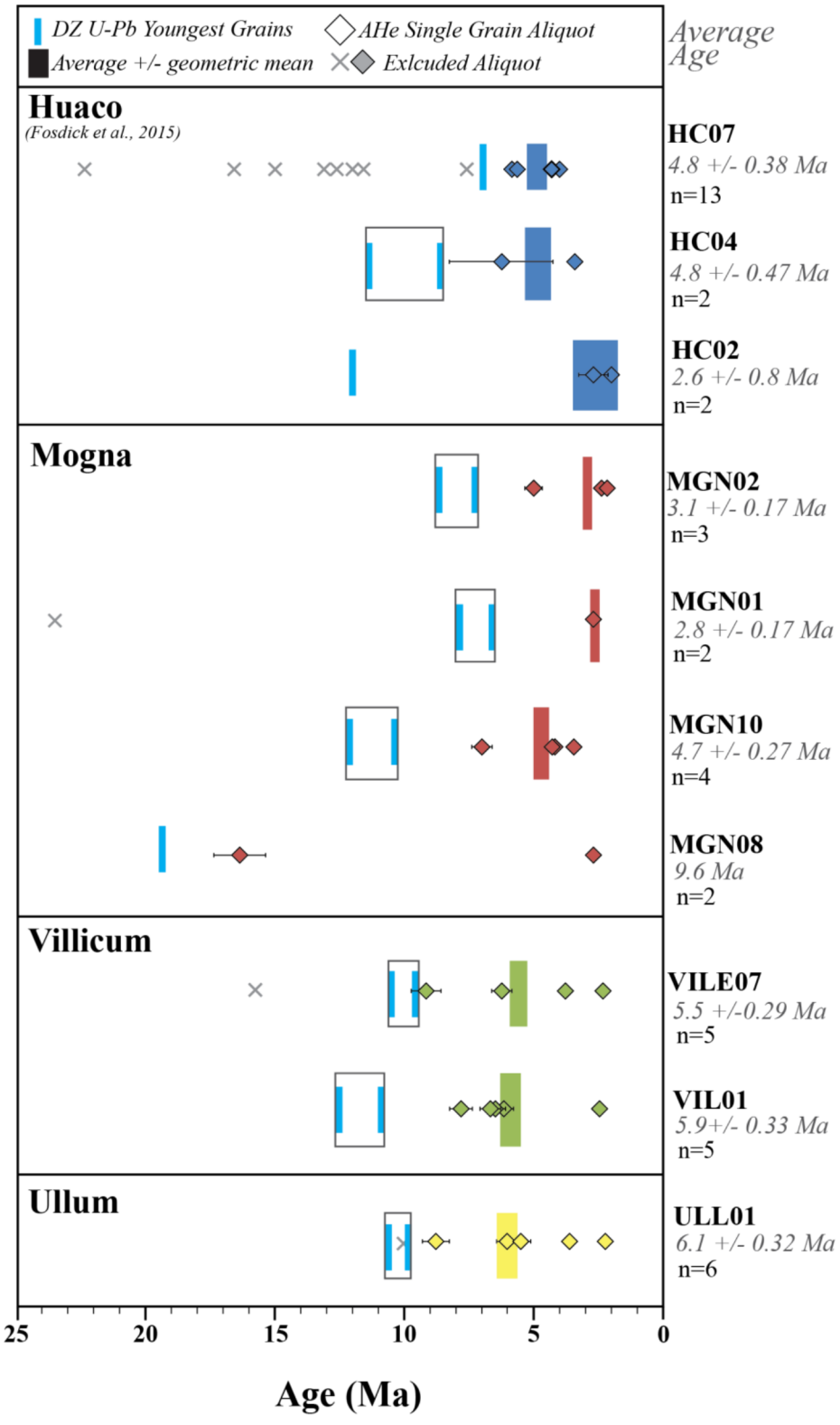

Figure 8: Plot of apatite (U-Th)/He ages for new Mogna, Villicum, and Ullum samples, and published Huaco samples (Fosdick et al., 2015). All (U-Th)/He ages are plotted with 2σ error bars. For each locality, samples are presented in stratigraphic order, with maximum depositional ages denoted by black boxes with teal bars as errors. Colored boxes represent mean (U-Th)/He age and error for all accepted aliquots.

6. PROVENANCE SYNTHESIS

Here we discuss the stratigraphic trends in paleocurrent measurements, detrital zircon U-Pb age populations, and conglomerate clast counts and how they may provide insight on erosional and related regional deformation across the various Andean ranges. Paleocurrent measurements from the Villicum and Ullum sections both record east-southeast directed sediment dispersal patterns, which suggest primarily western sediment source regions (i.e. Frontal Cordillera and Precordillera) during the Miocene and Pliocene. Paleocurrent measurements from the Huaco section also record southeast to east directed flow (Jordan et al., 2001). In the Mogna section, paleocurrent measurements from the basal deposits indicate an initial northwest directed flow that reversed up-section to an east directed flow throughout the Miocene and Pliocene (Capaldi et al., 2020).

Both Ullum and Villicum stratigraphic sections incorporate a range of Andean arc aged zircons (0-200 Ma) from 24% to 60% for the Villicum section and 14% to 43% for the Ullum section. It is important to note that > 90% of grains within the Andean arc age component are quite young, mainly falling in the Oligocene-Pliocene (32-4 Ma) time period. Neither of the southern Bermejo sections display consistent or obvious up-section trends in terms of Andean arc derived zircons, however, consistent incorporation of these young (Oligocene-Pliocene) grains likely tracks the eastward propagation of arc magmatism towards the foreland associated with the migrating flat slab (Kay and Mpodozis 2001; Capaldi et al., 2021). Deposition of Bermejo basin deposits is coeval with initiation of deformation within the Precordillera, so it must be noted that these young zircons may be recycled Andean arc grains sourced from deforming/uplifting basin deposits within the Precordillera.

Late Carboniferous to Triassic (225-330 Ma) aged zircon grains represent another steady contributor to Neogene basin fill of the southern Bermejo basin. Arc magmatism and crustal thickening (associated with input of the Andean arc zircons) was synchronous with deformation and erosion along the Frontal Cordillera (Fosdick et al., 2017; Buelow et al., 2018; Mackaman-Lofland et al., 2020). The deformation and associated erosion in the Frontal Cordillera likely exhumed Choiyoi-Elqui igneous rocks that acted as a significant provenance source to the Villicum and Ullum depocenters in southern Bermejo basin. There is a notable flux in late Carboniferous-Triassic zircons, *ca.* 10 Ma, potentially signaling (1) a pulse of Frontal Cordillera deformation at this time or (2) recycled zircon input from the actively deforming Cenozoic basin deposits (e.g. Pachaco, Talacasto, & Albarracin - west of Ullum and Villicum; Levina et al., 2014), which incorporated significant proportions of Choiyoi-aged zircon grains. Felsic and mafic volcanic clasts are also steady contributors to the conglomerate units in Bermejo basin, which are diagnostic of erosion of Paleozoic and Miocene volcanic rocks of the Frontal Cordillera (Jordan et al., 1993). Volcanic clast compositions range from 66% to 44%, reach maximum input at *ca.* 10 Ma, and generally decrease up-section, likely reflecting initiation of more proximal Precordillera deformation through time (and therefore less incorporation of Frontal Cordillera derived clasts).

Sierras Pampeanas aged zircons (380-725 Ma) generally increase up-section in the southern Bermejo sections with the exception of the basal sample at Ullum (ULL02), which records anomalously high percentage of Pampean grains at ~40%. This anomaly likely reflects incorporation of local Paleozoic strata in the earliest stage of basin deposition at the Ullum depocenter. The up-section increase in Eastern and Western Sierras Pampeanas aged zircon populations is particularly evident in the Villicum section and is most likely a result of increased sediment contribution from the Precordillera associated with unroofing of Paleozoic strata *ca.* 10

Ma (Jordan et al., 1993; Fosdick et al., 2015). Proterozoic basement zircons (925-1450 Ma) follow a similar trend to Pampean zircons - increasing up-section. It is likely that Precordillera deformation also contributed Proterozoic aged zircons into the basin fill in southern Bermejo basin. Metasedimentary and red-brown-gray sandstone conglomerate clasts follow similar up-section trends to Paleo-Proterozoic detrital zircon provenance, generally increasing up-section (with a few internal cycles). Metasedimentary and sandstone clasts record Precordillera deformation and represent the Paleozoic strata being unroofed and subsequently eroded and transported to the Bermejo basin. Paleozoic conglomerate clast compositions increase from ~30% to ~50% in southern Bermejo. Deposition of southern Bermejo basin sections is coeval with the initiation of deformation across the Precordillera and into the western-most foreland, and therefore it is possible that zircon grains deposited in Ullum and Villicum are recycled from older Cenozoic basins, and are simply recording that deformational sweep into the foreland (Levina et al., 2014).

6.1. Multidimensional Scaling Plot

We generated a MDS plot to examine the similarity among zircon provenance for each basin location (Fig. 8). New data from Villicum and Ullum is integrated with published detrital zircon U-Pb age datasets from the Mogna and Huaco sections (Fosdick et al., 2015; Amidon et al., 2017; Capaldi et al., 2020). The DZ samples plotted in the MDS exhibit trends that indicate the positive y-space represents greater abundance of Paleozoic arc and Proterozoic basement aged zircons; positive x-space represents greater influence of Choiyoi and Elqui arc diagnostic ages; and negative x-space represents greater incorporation of Andean arc aged zircon grains. Each U-Pb age distribution is also annotated with the approximate depositional age of the given sample, adding a time component to the plot (Fig. 8).

The MDS plot reveals several distinct spatial and temporal trends among the four depocenters indicating sediment dispersal connectivity or isolation during the foreland basin development. The samples from the Huaco section (Fig. 8; blue) plot further away from the other three sections, dictated by the strong older Paleozoic arcs and Proterozoic basement source age component observed in these samples. The cluster of Huaco samples in MDS space suggests that the Huaco depocenter recorded a unique sediment source that is fluvially disconnected from southern basin depocenters. This sediment source was likely being fed by recycled Pampean-Proterozoic zircons during northern Precordillera deformation, signaling a greater contribution of these grains in the north. The basal Mogna (Fig. 8; red) and Ullum (Fig. 8; yellow) samples also plot in the Pampean-Proterozoic basement MDS space, suggesting that local Paleozoic and basement sources that underlie the depocenters were contributing sediment in the initial basin formation phase. Both the Mogna and Villicum (Fig. 8; red and green) samples overlap predominantly in the negative-x MDS space, indicating a shared sediment source dominated by Andean arc derived grains. The amount of overlap observed between the zircon U-Pb age distributions of Mogna and Villicum after *ca.* 10 Ma implies that these sections were fluvially connected and tapping into an eroding Andean arc source. The dominant young (Oligocene-Pliocene) aged zircon being sourced to this Neogene basin fill suggest that the fluvial system feeding Mogna and Villicum was tapping into Cenozoic basins of the Precordillera which began deforming between 12-9 Ma (Jordan et al., 1993; Levina et al., 2014). The Ullum samples plot towards the positive x-space, suggesting a system that is more dominated by Carboniferous-Triassic (Choiyoi & Elqui arc) sources. There is a fair amount of overlap between the Mogna and Villicum system with Ullum, indicating that these sections experienced similar sediment provenance histories. However, Ullum experiences a greater influence of sediment input from the

Choiyoi and Elqui arcs suggesting that the system feeding into Ullum was fluvially disconnected from the source feeding Mogna and Villicum. Since sediment was depositing in the Ullum depocenter at roughly the same time as Villicum (13-6 Ma), this may suggest that the source for Ullum was a southern Cenozoic basin with a unique depositional history (e.g. Albarracin studied by Levina et al., 2014) which incorporated significant proportions of Choiyoi-Elqui igneous rocks. The observed along-strike differences in sediment provenance during Bermejo basin deposition is a direct result of the along-strike complexities seen within the deforming Precordillera coeval with deposition in the foreland.

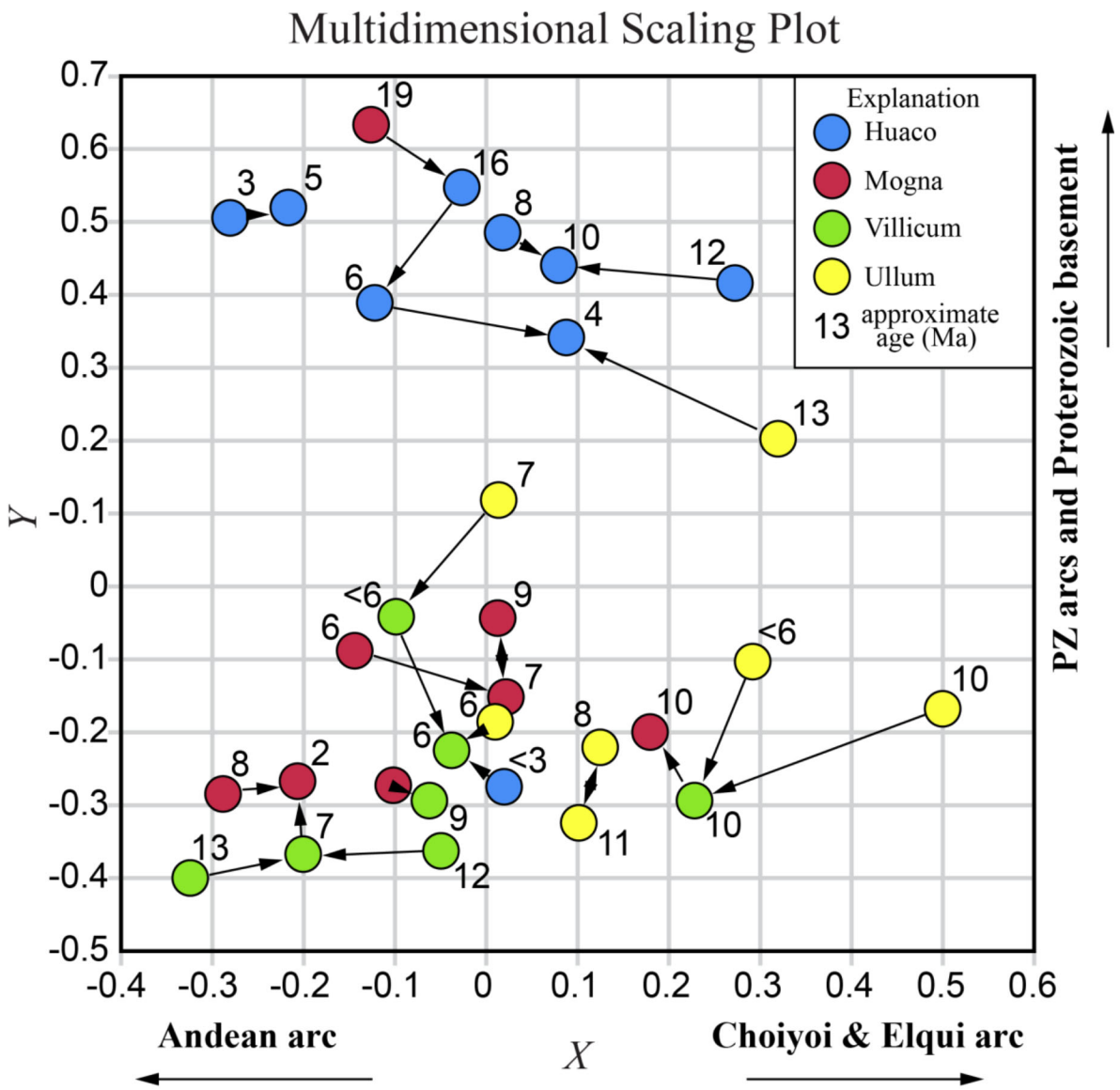

Figure 9: Three-dimensional multidimensional scaling (MDS) plot of DZ U-Pb age distributions generated for sandstone samples using KDE (20 Myr bandwidth) and R2 cross-correlation coefficient test. Lines represent nearest neighbor (black arrows). Axes are unitless with age distribution data trends on X and Y axis inferred (black arrows).

7. BASIN ANALYSIS

Integration of new detrital zircon U-Pb geochronologic time constraints (MDAs) from the Villicum and Ullum sections paired with published magnetostratigraphic data for the Huaco (Johnson et al., 1986) and Mogna (Milana et al., 2003) sections allows for a reconstruction of along-strike sediment accumulation histories of the Bermejo basin (Fig. 9). The stratigraphic age and thickness data reveal a distinct along-strike difference in sediment accumulation histories in northern Bermejo (Huaco, Mogna) versus southern Bermejo (Villicum, Ullum). First order observations show a decrease in stratigraphic thicknesses from north to south. Huaco, at the northern extent of our study, has a thickness greater than 5 km, while Ullum, at the southern extent, is less than 2 km thick (Fig. 9).

Sediment accumulation rates can be a useful tool for informing depositional environments, especially in a foreland basin system with well-defined depositional zones. In the early stages of deposition in northern Bermejo basin (18-13 Ma), the Huaco and Mogna depocenters record low rates of sediment accumulation of 38 m/Myr (Huaco) and 75 m/Myr (Mogna). Low sediment accumulation rates at this time likely signify deposition in the backbulge zone of a foreland basin system (Flemings & Jordan, 1989; DeCelles & Burden, 1992). Between 13-9 Ma, the accumulation rate in northern Bermejo increases to 234 m/Myr (Huaco) and 143 m/Myr (Mogna). Sediment begins to accumulate in southern Bermejo basin at this time with rates of 190 m/Myr in Villicum and 112 m/Myr in Ullum. Maximum sediment accumulation rates occur between 9 and 5 Ma across the entire Bermejo foreland basin with observed rates of: 768 m/Myr in Huaco, 463 m/Myr in Mogna, 338 m/Myr in Villicum, and 263 m/Myr in Ullum. The observed increase in sediment accumulation rate through time signals a transition into a foredeep depositional zone of the evolving foreland basin system (DeCelles & Giles, 1996). In the final stage of basin development

(5-0 Ma), sediment continues to accumulate in Huaco and Mogna until *ca*. 2 Ma with decreased rates of 400 m/Myr at Huaco and 281 m/Myr at Mogna. Deposition in the southern Bermejo depocenters ceased during this stage. These decreased rates of sediment accumulation indicate a more proximal orogenic wedge and a switch to wedge-top deposition as the topographic front and associated foreland basin system continues to migrate eastward (Allmendinger and Judge, 2014; Fosdick et al., 2015; Mardonez et al., 2020; Mackaman-Lofland et al., 2022).

New AHe cooling ages from Mogna, Villicum, and Ullum depocenters along with published ages from Huaco (Fosdick et al., 2015), reveal two distinct phases of exhumation associated with exhumation along the Eastern Precordillera (Fig 9; gray bars). Collectively, the ages show a northward migration in basin cooling that initiates in southern Bermejo *ca*. 6 Ma followed by a second pulse at *ca*. 3 Ma in northern Bermejo. When stratigraphic age, thickness, and exhumation data are plotted together (Fig. 9), it becomes evident that the termination of deposition in the northern and southern sections aligns well with initiation of exhumation in the Eastern Precordillera.

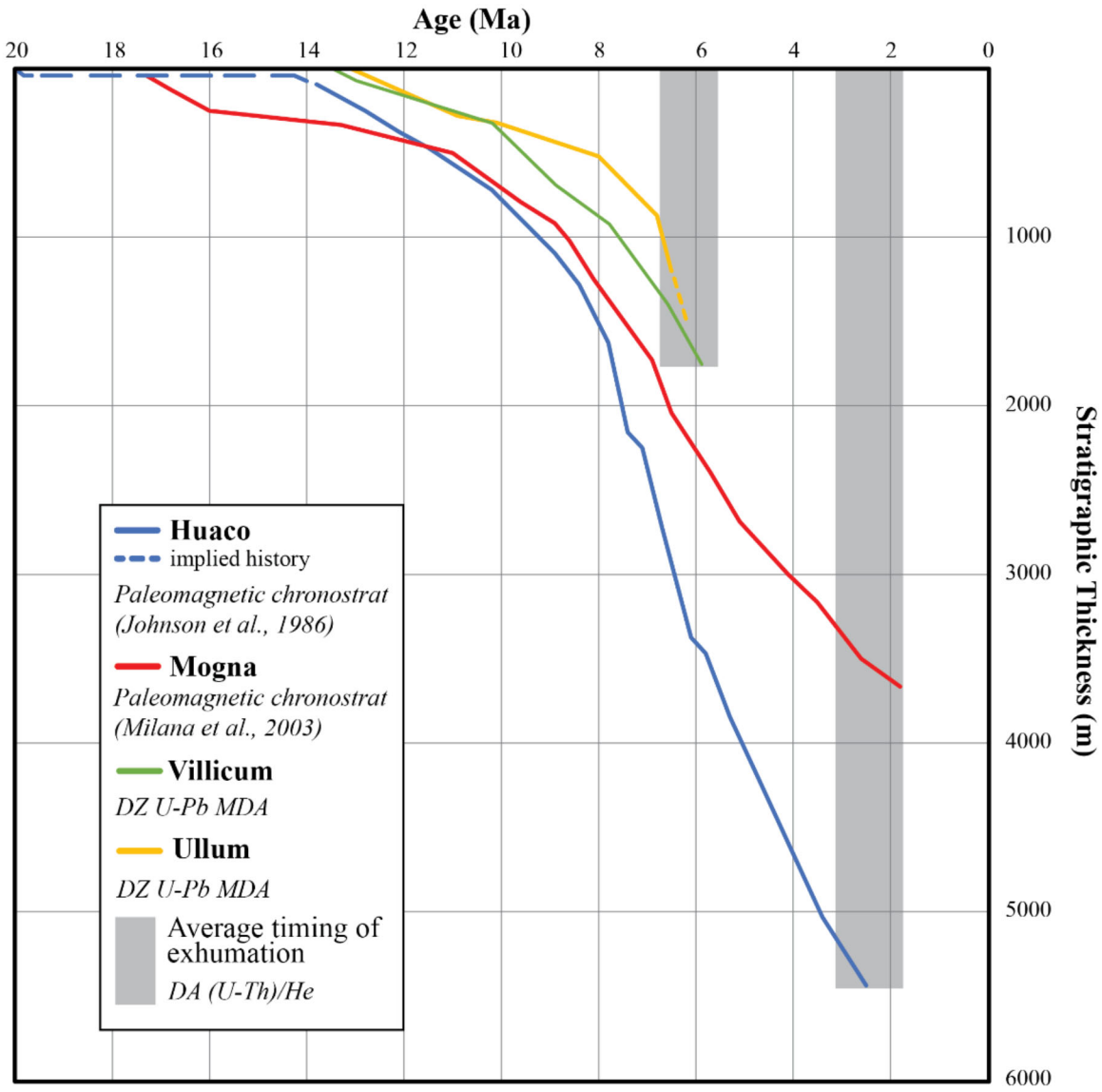

Figure 10: Cenozoic sediment accumulation history for Huaco, Mogna, Villicum, and Ullum depocenters in the Bermejo basin.

8. DISCUSSION

The combination of stratigraphic (Fig. 4), lithofacies (Table 1), provenance (Figs. 6 and 8), exhumation (Fig. 7) and accumulation (Fig. 9) histories allows us to provide insights on Andean unroofing patterns and the related depositional and deformational variations observed along strike within the Bermejo basin. We identify four key timesteps in the evolution of the Bermejo foreland basin: (1) Early to middle Miocene, 18-13 Ma; (2) Middle to Late Miocene, 13-9 Ma; (3) Late Miocene to early Pliocene, 9-5 Ma; and (4) Pliocene to present, 5-0 Ma (Fig. 10).

8.1. Phase I: Early-Middle Miocene

The early-middle Miocene stage of foreland basin development (18-13 Ma) is concentrated in northern Bermejo basin with basal depositional ages of *ca.* 16 Ma and 17 Ma for Huaco and Mogna, respectively (Milana et al., 2003; Mackaman-Lofland et al., 2022). Early sediment accumulates at very low rates (<80 m/Myr) in the northern Bermejo depocenters. Phase I records the initial development of the flexural foreland basin initiated by the eastward thrust-front advance across the Precordillera (Fernandez et al., 1996; Jordan et al., 1993; Milana et al., 2003). Sedimentological analyses of early-middle Miocene strata suggests earlier eolian depositional environments with a switch to more fluvially dominated systems by the end of phase I, preserved in the Rio Salado and Quebrada del Jarillal Formations (Fig 3; Fernandez et al., 1996; Jordan et al., 2001). The southern Bermejo depocenters record no sediment accumulation at this time, defining a non-depositional zone south of 31°S in Bermejo basin (Fig. 10). Southwest of the inactive southern Bermejo depocenters (Ullum and Villicum), the Miocene Albarracin basin began accumulating sediment between *ca.* 18-16 Ma (Levina et al., 2014; Verges et al., 2001). This indicates that deposition was occurring south of 31°S, but not in the eastern-most reaches of the Eastern Precordillera/southern Bermejo basin at Ullum and Villicum. Early to mid-Miocene

paleocurrent data indicate northwest directed flow for the Mogna section (Capaldi et al., 2020) and southwest directed flow for the Huaco section (Fosdick et al., 2017), suggesting initial sediment sources from the eastern cratonic margin and overlying Carboniferous to Triassic strata. Evidence of very low sediment accumulation rates of sediments derived from eastern cratonic sources suggests deposition in the back-bulge depositional zone of a foreland basin system (DeCelles and Giles, 1996). The lack of sediment accumulation in southern Bermejo during phase I suggests that either: (1) early exhumation in the Western-Central Precordillera was concentrated north of 31°S, and/or (2) the southern Bermejo basin remained a paleo-topographic high at this time.

8.2. Phase II: Mid-Late Miocene

The mid-late Miocene (13-9 Ma) phase in Bermejo basin development is marked by an increase in fluvial activity across the region and a notable reversal in paleocurrents from northwest-southwest to south-southeast directed flow at Mogna and Huaco (Capaldi et al., 2020; Fosdick et al., 2017) and the beginning of south-southeast directed flow at Villicum and Ullum. The Villicum and Ullum sections of southern Bermejo begin accumulating sediment at *ca.* 13 Ma, coinciding with the advance of the fold-thrust belt into the Central Precordillera between *ca.* 14-9 Ma (Fernandez et al., 1996; Jordan et al., 1993; Milana et al., 2003; Levina et al., 2014). Depositional environments during phase II of Bermejo basin development reflect ephemeral lake systems and distal floodplains that progressively grade into thicker and sandier fluvial facies recorded in the Lomas de las Tapias, Quebrada del Jarillal, Huachipampa, and Quebrada del Cura Formations. All four along-strike sections within the Bermejo basin experience relatively moderate sediment accumulation rates (~100-200 m/Myr) during the mid-late Miocene (Fig. 9). Both Huaco and Mogna depocenters record an increase from phase I, reflecting increased tectonic activity in the Precordillera. Observed moderate sediment accumulation rates and the occurrence of regional

fluvial activity sourced from western Andean regions indicates a distal foredeep depositional zone of the evolving foreland basin system (Fernandez et al., 1996; DeCelles and Giles, 1996). Mid-late Miocene Bermejo basin experiences a notable increase in late Carboniferous-Triassic aged zircon input and high contribution of felsic-mafic volcanic clasts, likely reflecting erosion of the Frontal Cordillera sources and or unroofing of foreland basin deposits across the Precordillera recycling the Andean arc and hinterland sediment signatures. Given the complexity of deformation within the entire Andean orogenic system at this time, it is likely that accumulating sediment in the Bermejo basin is being sourced from both the Frontal Cordillera and Precordillera (Jordan et al., 1993; Capaldi et al., 2020).

8.3. Phase III: End Miocene-Early Pliocene

The end Miocene-early Pliocene time (9-5 Ma) in the Bermejo basin is distinguished by increased sediment accumulation rates across the entirety of the foreland basin (~300 m/Myr in southern Bermejo to ~800 m/Myr in northern Bermejo). The observed contemporaneous increase in sedimentation rates at Huaco and Mogna (Fernandez et al., 1996) and Villicum and Ullum indicates progressive deformation in the eastern Central Precordillera (Jordan et al., 1993). Changes in lithofacies at Villicum and Ullum during this phase of basin development reflects the eastward advance of the Precordillera fold-thrust belt via increasingly coarser-grained sediments which is interpreted as a transition from avulsing sandy channels on a distal flood-plain to a higher-energy braided system and eventual incorporation of debris flow deposits (Upper Lomas de las Tapias, Mogna and El Corral Formations). Facies analyses of the Villicum and Ullum sections lead us to interpret the up-section trends as deposition and migration of a fluvial megafan that is being sourced from the actively deforming Precordillera thrust belt. Analysis of correlative formations in northern Bermejo have been interpreted as proximal alluvial fan and bajada

depositional environments (Fernandez et al., 1996; Johnson et al., 1986; Jordan et al., 1993), however we suggest that they may be a part of the separate fluvial megafan system. High sediment accumulation rates paired with sediment sourced directly from the approaching fold-thrust belt and dominant fluvial megafan facies implies that deposition is occurring in the foredeep depozone of the foreland basin system at this time (DeCelles and Giles, 1996; Flemings and Jordan, 1989). By *ca*. 6.5 Ma, southern Bermejo depocenters (Villicum and Ullum) briefly experience wedge-top deposition, evident by predominantly coarse-grained conglomerate facies (Mogna and El Corral Formations; DeCelles and Giles, 1996) before being incorporated into the fold-thrust belt by *ca*. 5 Ma. Detrital zircon U-Pb age distributions during phase III of Bermejo basin development reflect an increase in Paleozoic-Proterozoic age components further indicating unroofing of Paleozoic sediments within the Precordillera. Our new AHe data from the southern Bermejo sections reflect exhumation between 7-5 Ma, while northern Bermejo continues to accumulate sediment at this time in broad fluvial megafan depositional environments. The 3 to 5 Myr difference in the time of exhumation between the southern and northern Bermejo basin implies asynchronous evolution of the retroarc basin system, where deformation initiates in the Eastern Precordillera around 6 Ma in Ullum and Villicum. As a result of the evolving Eastern Precordillera thrust front, developing broad synclinal structures perturbed the Ullum and Villicum depocenters.

8.4. Phase IV: Pliocene to Present

The final phase of Bermejo basin development (5-0 Ma) is distinguished by basement-shortening in the foreland and consequent uplift of the Sierras Pampeanas basement ranges resulting in the present day broken-foreland basin system (Jordan and Allmendinger, 1986; Jordan et al., 2001; Horton et al., 2022). Sediment accumulation continues at Huaco and Mogna until *ca.* 4-2 Ma, with rates decreasing from the main phase of accumulation (9-5 Ma) to ~400 and ~300

m/Myr for Huaco and Mogna, respectively. Relatively high accumulation rates suggest continued deformation in the Precordillera, however the decrease in rates from the previous phase likely tracks the encroachment of the thrust front and deposition in the wedge-top foreland basin depozone (DeCelles and Giles, 1996). Deposition in northern Bermejo is dominated by thick conglomeratic facies (Mogna and El Corral Formations) corresponding to proximal river dominated fans (Fernandez et al., 1996; Jordan et al., 1993; Milana et al., 2003), which we interpret as likely fluvial megafan systems. Northern Bermejo exhumation initiates during phase IV, coeval with uplift of the Sierras Pampeanas. Published AHe ages for the Huaco section suggest uplift at *ca*. 2 Ma (Fosdick et al., 2015) and new data from the Mogna section shows exhumation initiating *ca*. 3.5 Ma, at which point northern Bermejo is incorporated in the fold-thrust belt, forming the broad anticlinal structures observed today at Mogna and Huaco. The contemporaneous deformation of northern Bermejo and the thick-skinned Sierras Pampeanas lead us to believe that the northern Eastern Precordillera may be kinematically linked to the deep-rooted thrust structures of the Sierras Pampeanas, as suggested previously (e.g. Zapata and Allmendinger, 1996; Ramos et al., 2002; 2009; Siame et al., 2002; 2005; Verges et al., 2007). The earlier uplift of southern Bermejo (>5 Ma) lead us to conclude that there are complex along-strike variations in the Eastern Precordillera thrust-front evolution, and that southern Bermejo basin may not be structurally linked to the deep-rooted Sierras Pampeanas, as previously suggested. We support a potential thin-skinned model where initial Eastern Precordillera thin-skinned thrust sheets are refolded by later basement (thick-skinned) deformation (e.g. Meigs et al., 2006). Some fold-thrust belts experience both thin and thick-skinned structural styles in different portions of the belt, sometimes changing along strike (Lacombe and Bellahsen, 2016; Parker and Pearson, 2021). The overlap of these structural styles has primarily been observed near the foreland, where thin-skinned and thick-

skinned thrust domains converge towards one another (Parker and Pearson, 2021). We suggest the possibility of variable structural styles of deformation along-strike in the Eastern Precordillera, however further work is required.

This is the first time that along-strike variations in both the depositional and deformational history of Neogene Bermejo basin deposits has been constrained and we highlight specific differences north and south of 31ºS. New sedimentological, geochronologic, and thermochronologic datasets provide quantitative evidence of the variability that exists in retroarc foreland basin development and thrust-front evolution in the south-central Andes between 30-32ºS.

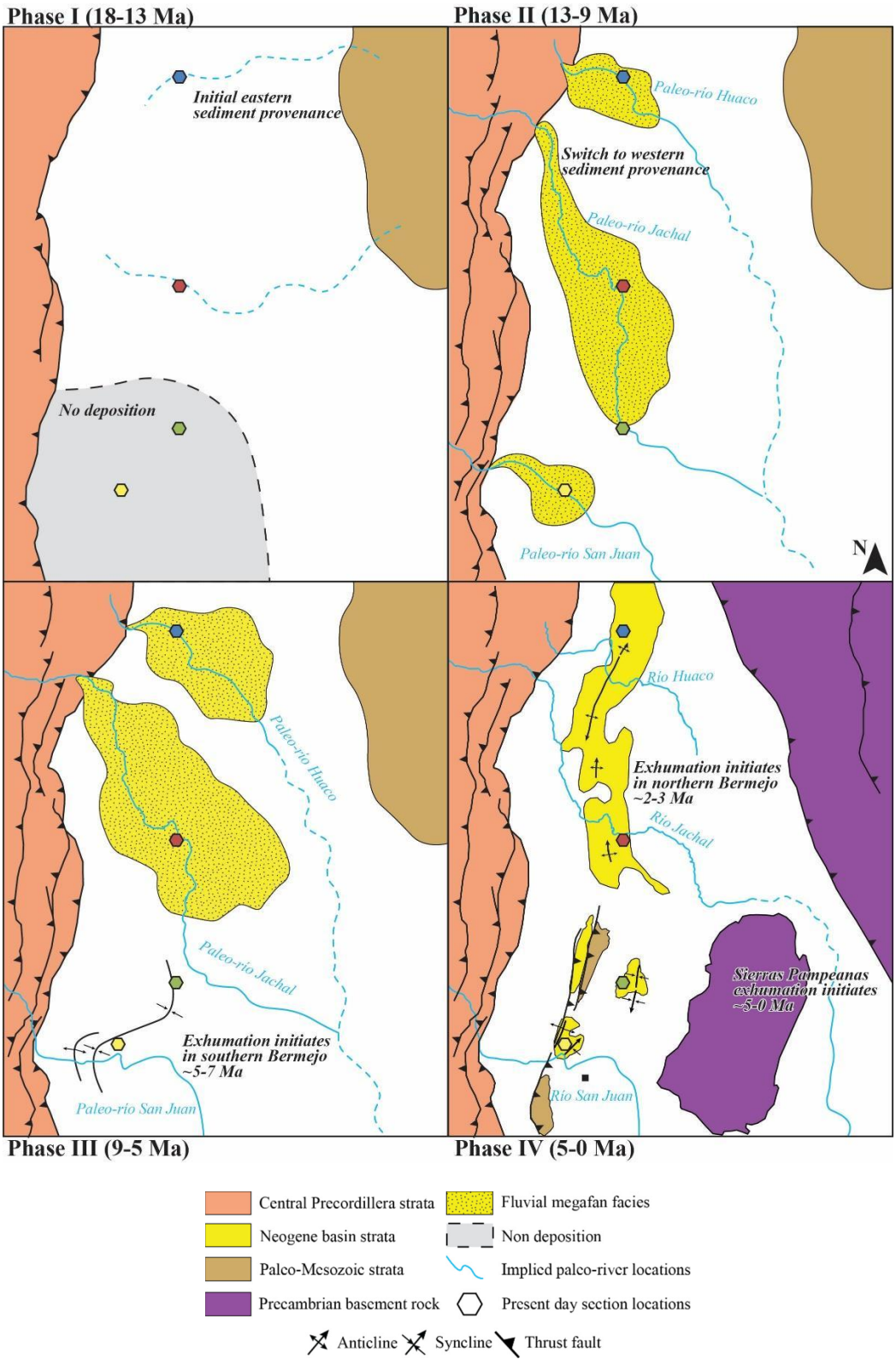

Figure 11: Simplified paleogeographic reconstruction of Bermejo basin evolution between 18-0 Ma. Phase I-IV are described in detail in discussion subsections 8.1-8.4. Stratigraphic sections: Blue = Huaco, Red = Mogna, Green = Villicum, & Yellow = Ullum.

9. CONCLUSIONS

The Bermejo retroarc foreland basin formed as a flexural response to Miocene crustal thickening in the Andean orogenic system, specifically the eastward propagating Precordillera fold-thrust belt and the basement-involved uplift of the Sierras Pampeanas. The well-preserved stratigraphy of Neogene basin deposits in the Bermejo basin provide an ideal opportunity for an along-strike analysis of the evolution of the adjacent Eastern Precordillera and overall foreland basin-broken basin development in a flat-slab subduction region. Integration of new and published datasets allows for a temporal and spatial analysis of basin development and deformation to understand the variability in an evolving thrust front.

1. Published data from northern Bermejo basin deposits places temporal constraints on deposition between *ca.* 20-2 Ma while new data from southern Bermejo basin deposits shows deposition between *ca.* 13-6 Ma. The northern Bermejo basin experiences a longer-lived depositional history, accumulating thicker stratigraphic sections (>4km) than in the south (<2km).
2. Facies analyses of southern Bermejo stratigraphy identify upward coarsening sequences dominated by thick, multistoried, laterally continuous sand channels with flat bottoms, interbedded with mud-siltstone floodplain and overbank facies that are capped by thick conglomerate braided river channels. This stratigraphic succession is interpreted to represent a fluvial megafan sequence being sourced by the Precordillera and Andean hinterland. The upward coarsening and thickening trend of stratigraphic sections tracks the migration of the fluvial megafan system as the Precordillera thrust-front propagates into the foreland.

3. Detrital zircon U-Pb geochronologic analyses paired with conglomerate clast composition datasets provide insight on sediment provenance through time, which can detect deformation and erosion of distinct source areas. Up-section trends of significant pulses of certain age components and clast lithologies inform on regional deformation. In southern Bermejo basin, provenance synthesis detects up-section increases in both (1) Paleoproterozoic zircon age components, and (2) Paleozoic metasedimentary and sedimentary conglomerate clasts, indicating a pulse of Precordillera deformation between 13 and 6 Ma. There is also a notable increase in late Carboniferous-Triassic aged zircons and a high percentage of volcanic conglomerate clasts *ca.* 10 Ma, which signals either (1) a pulse of deformation in the Frontal Cordillera, or (2) exhumation of Cenozoic basin fill to the west, at this time.
4. New AHe data for northern (Mogna) and southern (Villicum and Ullum) Bermejo basin localities, along with published AHe ages for Huaco show two distinct pulses of exhumation related cooling in the Bermejo basin. The Eastern Precordillera fold-thrust belt deformation incorporated the southern Bermejo basin strata at *ca.* 6 Ma. Eastern Precordillera exhumation migrated northward to the Mogna depocenter at *ca.* 3.5 Ma and to the Huaco depocenter by 2 Ma. The time transgressive trend in exhumation along strike of the Bermejo basin implies diachronous deformation of basin deposits.
5. Combined analysis of sedimentologic, geo-thermochronologic, and basin history suggest that the along-strike evolution of the Bermejo foreland basin system has been asynchronous through time. We use observed trends and available data to suggest that the southern Eastern Precordillera deformation is kinematically linked to the thin-skinned Central Precordillera and the northern Eastern Precordillera is kinematically linked to the

basement-involved Sierras Pampeanas. Further work is needed to assess the causes of this regional variation in the Neogene thrust front evolution.

Appendix A: Conglomerate clast count field data for southern Bermejo stratigraphic sections.

Lithology	ULLCC01	%	ULLCC02	%	ULLCC03	%	ULLCC04	%	ULLCC05	%	ULLCC06	%	ULLCC07	%	ULLCC08	%	ULLCC09	%
	175		320		525		635		877		1026		1208		1344		1500	
Maroon/brown volcanic	30	20	23	17	20	14	25	15	25	15	28	19	21	14	20	12	11	8
Red/orange volcanic	38	25	40	29	25	18	32	20	38	23	23	15	37	24	37	22	31	21
Green volcanic	20	13	14	10	7	5	13	8	22	13	14	9	18	12	18	10	7	5
Andesite	2	1	2	1	1	1	2	1	2	1	10	7	5	3	10	6	6	4
Green siltstone	37	25	45	32	72	52	70	43	51	31	45	30	52	34	62	36	65	45
Tan siltstone	4	3	3	2	1	1	5	3	4	2	2	1	0	0	2	1	5	3
Black volcanic w/ phenocrysts	7	5	0	0	3	2	3	2	2	1	0	0	3	2	9	5	11	8
Vein quartz	3	2	4	3	0	0	3	2	1	1	4	3	1	1	1	1	1	1
Black chert	0	0	0	0	0	0	0	0	0	0	0	0	0	0	0	0	1	1
Granite	1	1	0	0	0	0	0	0	4	2	3	2	10	6	5	3	4	3
Grey limestone	0	0	0	0	0	0	0	0	0	0	0	0	0	0	0	0	0	0
Grey volcaniclastic	2	1	0	0	4	3	2	1	4	2	2	1	0	0	0	0	0	0
Brown siltstone	0	0	7	5	4	3	7	4	8	5	15	10	5	3	5	3	1	1
Grey sandstone	0	0	0	0	0	0	0	0	0	0	0	0	1	1	2	1	2	1
other	6	4	1	1	1	1	2	1	2	1	3	2	1	1	1	1	1	1
total	150		139		138		164		163		149		154		172		146	

Lithology	VILE CC01	%	VILE CC02	%	VILE CC03	%	VILE CC04	%	VILE CC05	%	VILE CC06	%	VILE CC07	%	VILE CC08	%
Height	0.5		194.5		623		773		937		1387		1671		1778	
Maroon/Brown vol	0	0	103	29	58	40	69	46	42	34	40	35	58	35	38	28
Orange/Red Vol	0	0	53	15	17	12	25	17	33	27	14	12	31	19	18	13
Green Vol	0	0	98	27	15	10	15	10	7	6	4	4	11	7	6	4
Grey Vol/Andesite	0	0	29	8	5	3	6	4	2	2	1	1	0	0	0	0
Black Vol/ Phenocryst	0	0	0	0	15	10	1	1	2	2	0	0	6	4	5	4
Vein quartz	0	0	0	0	6	4	2	1	3	2	1	1	1	1	0	0
Granite	0	0	0	0	0	0	0	0	0	0	1	1	10	6	13	10
Black Chert	16	8	0	0	0	0	0	0	0	0	0	0	0	0	0	0
green sand-siltstone	35	18	42	12	26	18	31	21	33	27	52	46	50	30	54	40
Brown sand-siltstone	0	0	6	2	0	0	0	0	0	0	0	0	0	0	0	0
tan siltstone	0	0	0	0	0	0	0	0	0	0	0	0	0	0	0	0
red sandstone	0	0	0	0	0	0	0	0	0	0	0	0	0	0	0	0
VC-Sand calcite cement	0	0	27	8	0	0	0	0	0	0	1	1	0	0	1	1
Quartzite	0	0	0	0	0	0	0	0	0	0	0	0	0	0	0	0
blue-grey limestone	63	32	0	0	0	0	0	0	0	0	0	0	0	0	0	0
White/grey Dolomite	83	42	0	0	0	0	0	0	0	0	0	0	0	0	0	0
phyllite/ meta rock	0	0	0	0	0	0	0	0	0	0	0	0	0	0	0	0
other	2	1	1	0	3	2	1	1	0	0	0	0	0	0	0	0
total	199		359		145		150		122		114		167		135	

Appendix B: Paleoflow field measurements for southern Bermejo stratigraphic sections.

Station	ULL PF01		ULL PF03		ULL PF04		ULL PF05		ULL PF07		ULL PF08		ULL PF09		ULL PF10	
Height (m)	179		525		635		877		1115		1208		1344		1455	
Bedding S/D	357	56	38	51	47	30	31	34	34	40	34	40	31	40	31	40
Imbricated clast S/D	S	D	S	D	S	D	S	D	S	D	S	D	S	D	S	D
	316	59	37	40	204	33	201	35	282	61	3	37	242	18	257	7
	300	49	57	22	269	16	188	23	245	38	349	19	288	23	104	38
	303	45	9	25	245	10	217	23	287	63	0	38	103	12	139	45
	179	89	41	34	197	24	123	13	300	40	11	42	136	18	152	38
	356	49	20	39	16	42	103	17	307	46	295	35	119	28	107	36
	339	88	35	58	272	19	144	15	317	17	303	43	115	39	156	31
	53	57	32	43	346	23	89	28	256	34	13	33	327	4	223	24
	47	73	29	48	273	25	213	51	276	35	293	26	391	14	210	20
	45	56	18	55	298	24	112	11	343	27	314	38	81	28	222	24
	29	65	19	43	308	34	127	13	328	33	194	20	57	26	155	37
	34	73	22	40	311	25	149	6	293	28	147	12	117	14	153	28
	30	64	68	34	310	39	311	12	175	10	262	39	176	37	241	16
	358	80	183	77	342	36	269	10	136	19	267	54	149	20	215	39
	4	81	20	74	285	52	255	9	277	24	261	25	115	30	328	23
	354	76	36	28	301	18	333	40	277	39	335	23	327	25	106	25
			45	39	34	9	335	29	290	26	344	22	38	28	117	33
			3	40	183	24	323	42	257	47	316	30	291	29	204	23
			39	58	177	24	332	47	288	40	4	30	83	27	13	50
			77	70	157	17	343	35	336	58	255	28	82	33	12	36
			46	76	320	16	333	18	342	34	329	8	82	37	208	17
			78	73			303	31	15	40	331	10	267	28	105	22
			45	71			286	25	334	52	254	15	254	30	326	21
			44	66			185	30	315	17	335	36	267	34		
			69	43			234	36	344	56	324	29	158	18		
			36	66			260	28	12	53	351	30	152	27		
			47	67					40	45						
			34	64					43	36						
			63	41					24	53						

			51	75					357	57						
			23	47					352	57						

Station	VILE PF01		VILE PF06		VILE PF07		VILE PF08	
Height (m)	0.5		1389		1671		1768	
Bedding S/D	0	21	40	10	40	10	40	10
Imbricated clast S/D	S	D	S	D	S	D	S	D
	179	52	357	34	270	16	190	25
	162	24	2	30	231	23	240	45
	166	20	10	27	266	20	245	52
	234	19	6	25	230	29	210	37
	225	31	8	28	257	12	160	45
	153	36	10	21	205	22	210	27
	152	19	0	38	114	20	10	25
	230	24	19	37	204	28	5	36
	204	21	14	43	222	29	260	15
	213	25	11	46	184	37	10	4
	250	49	357	35	213	55	160	35
	272	22	10	44	194	32	150	33
	256	30	350	30	183	40	12	15
	251	28	320	25	252	32	140	30
	204	48	322	24	183	35	180	24
	234	20						
	246	23						
	275	14						
	206	48						

	266	59						

Appendix C: Maximum depositional age calculations for southern Bermejo detrital zircon U-Pb samples.

	Maximum Depositional Age Calculations								
	youngest single grain (YSG)			Youngest three zircons (Y3Z)			Youngest grain cluster at 2σ (YGC 2σ)		
sample	age	error	% disc	age	error	% disc	age	error	% disc
ULL01	**10.2**	**0.5**	11.9	10.2	0.5	11.9	10.2	0.5	11.9
				10.8	0.6	0.5	10.8	0.6	0.5
				10.8	0.5	6.4	10.8	0.5	6.4
				10.6	**0.3**		10.8	0.9	17.1
							10.6	**0.2**	
ULL02	**12.7**	**1.4**	0.3	12.7	1.4	0.3	12.7	1.4	0.3
				13.0	1.1	12.4	13.0	1.1	12.4
				13.0	1.9	38.6	13.0	1.9	38.6
				12.9	**0.3**		13.3	2.5	5.8
							13.4	1.3	13.6
							13.4	1.9	23.5
							13.1	**0.2**	
ULL03	**10.5**	**1.3**	44.3	10.5	1.3	44.3	10.5	1.3	44.3
				10.5	0.6	0.4	10.5	0.6	0.4
				10.8	0.7	12.8	10.8	0.7	12.8
				10.6	**0.1**		11.2	0.8	3.7
							11.3	0.9	17.0
							10.9	**0.3**	
ULL04	**9.0**	**1.5**	38.0	9.0	1.5	38.0	9.0	1.5	38.0
				10.6	1.7	48.1	10.6	1.7	48.1
				10.8	2.0	42.2	10.8	2.0	42.2
				10.1	**0.8**		**10.1**	**0.8**	
ULL05	**7.8**	**0.7**	16.0	7.8	0.7	16.0	7.8	0.7	16.0
				7.9	1.3	26.5	7.9	1.3	26.5
				8.0	0.9	39.6	8.0	0.9	39.6

				7.9	**0.1**		8.1	1.4	46.8
							8.4	0.9	5.6
							8.0	**0.2**	
ULL06	**6.8**	**0.9**	15.3	6.8	0.9	15.3	**6.8**	**0.9**	15.3
				14.9	2.3	15.2			
				18.4	2.0	4.6			
				13.4	**4.9**				
ULL07	**6.5**	**0.4**	15.7	6.5	0.4	15.7	**6.5**	**0.4**	15.7
				10.0	0.9	5.4			
				12.5	1.7	4.1			
				9.7	**2.4**				
ULL08	**8.2**	**1.4**	42.5	8.2	1.4	42.5	8.2	1.4	42.5
				8.3	1.4	24.1	8.3	1.4	24.1
				8.3	1.6	34.8	8.3	1.6	34.8
				8.3	**0.0**		**8.3**	**0.0**	
VIL01	**11.6**	**0.9**	5.8	11.6	0.9	5.8	11.6	0.9	5.8
				12.3	1.0	6.1	12.3	1.0	6.1
				14.0	0.7	18.4	**11.9**	**0.4**	
				12.6	**1.0**				
VILE04	**12.8**	**0.8**	5.3	12.8	0.8	5.3	12.8	0.8	5.3
				13.6	1.7	13.4	13.6	1.7	13.4
				13.6	1.0	18.6	13.6	1.0	18.6
				13.3	**0.4**		**13.3**	**0.4**	
VILE05	**12.4**	**0.8**	9.0	12.4	0.8	9.0	12.4	0.8	9.0
				12.4	1.0	1.7	12.4	1.0	1.7
				12.8	0.8	11.2	12.8	0.8	11.2
				12.5	**0.2**		12.8	2.5	14.1
							12.8	1.0	8.4
							13.2	0.8	7.4
							13.2	1.5	17.0
							12.8	**0.3**	

VILE07	**10.0**	**0.6**	2.6	10.0	0.6	2.6	10.0	0.6	2.6
				10.0	0.5	14.1	10.0	0.5	14.1
				10.8	0.6	29.9	**10.0**	**0.0**	
				10.2	**0.4**				
VILE08	**8.3**	**0.8**	4.8	8.3	0.8	4.8	8.3	0.8	4.8
				8.4	0.5	14.7	8.4	0.5	14.7
				8.7	1.2	0.0	8.7	1.2	0.0
				8.4	**0.2**		8.7	0.8	29.6
							8.7	0.4	11.8
							8.8	0.9	7.9
							8.8	0.4	11.7
							8.9	0.9	33.5
							9.0	0.7	13.3
							8.7	**0.2**	
VILE09	**7.1**	**0.8**	24.5	7.1	0.8	24.5	7.1	0.8	24.5
				7.2	1.0	19.7	7.2	1.0	19.7
				7.4	0.8	44.2	7.4	0.8	44.2
				7.2	**0.1**		7.5	0.9	14.6
							7.5	0.8	29.4
							7.6	1.3	16.5
							7.6	0.9	17.4
							7.7	0.9	35.2
							8.0	0.6	3.4
							8.0	1.0	33.9
							8.2	0.8	1.8
							7.6	**0.3**	
VILE10	**6.4**	**0.4**	7.7	6.4	0.4	7.7	**6.4**	**0.4**	7.7
				8.4	0.7	20.1			
				8.5	0.4	23.2			
				7.7	**1.0**				
VILE11	**5.7**	**0.6**	38.4	5.7	0.6	38.4	**5.7**	**0.6**	38.4

				7.6	0.6	18.3			
				8.0	0.5	13.7			
				7.1	**1.0**				

Appendix D: Reduced (U-Th[Sm])/He data for Mogna, Villicum and Ullum Detrital Apatite thermochronology samples.

Reduced (U-Th[Sm])/He Data												
Sample	**mineral**	**Age, Ma**	**err., Ma**	**U (ppm)**	**Th (ppm)**	**147Sm (ppm)**	**[U]e**	**Th/U**	**He (nmol/g)**	**mass (ug)**	**Ft**	**ESR**
MGN01-1	apatite	2.8	0.17	2.5	5.6	99.4	4.3	2.22	0.0	1.10	0.56	33.85
MGN01-2	apatite	33.9	2.04	9.3	27.6	99.0	16.2	2.95	2.0	1.98	0.64	43.01
MGN01-3	apatite	23.9	1.43	21.6	55.5	154.3	35.1	2.57	3.4	4.52	0.73	57.97
MGN02-1	apatite	2.4	0.14	4.0	10.9	164.4	7.3	2.73	0.0	0.56	0.47	27.07
MGN02-2	apatite	31.6	1.90	20.1	25.9	336.3	27.7	1.29	2.5	0.60	0.50	28.45
MGN02-3	apatite	31.0	1.86	33.1	22.2	243.8	39.4	0.67	4.0	1.16	0.60	35.96
MGN02-4	apatite	5.0	0.30	4.0	10.4	164.5	7.2	2.60	0.1	0.70	0.50	28.61
MGN02-5	apatite	2.1	0.12	8.3	22.1	149.1	14.1	2.66	0.1	0.27	0.35	20.85
MGN08-1	apatite	46.9	2.81	10.3	14.3	50.0	13.8	1.39	2.3	1.61	0.63	40.80
MGN08-2	apatite	61.3	3.68	5.1	20.5	304.3	11.3	4.05	2.2	0.72	0.53	31.78
MGN08-3	apatite	16.4	0.99	24.7	25.5	122.8	31.1	1.04	1.5	0.75	0.54	31.25
MGN08-6	apatite	2.7	0.16	4.0	13.8	16.8	7.2	3.48	0.1	2.05	0.65	44.83
MGN10-1	apatite	7.0	0.42	6.7	16.1	81.3	10.9	2.39	0.3	2.41	0.67	46.33
MGN10-3	apatite	133.2	7.99	9.5	19.3	103.6	14.4	2.04	6.5	1.39	0.61	38.31
MGN10-6	apatite	3.5	0.21	2.4	3.6	118.4	3.8	1.55	0.1	1.90	0.65	42.73
MGN10-8	apatite	4.2	0.25	2.4	7.9	100.9	4.7	3.36	0.1	2.86	0.69	49.69
MGN10-9	apatite	4.1	0.25	6.0	20.3	112.8	11.2	3.38	0.2	3.64	0.70	52.33
ULL01-2	apatite	10.1	0.61	2.0	12.7	133.8	5.5	6.48	0.1	0.43	0.42	24.41
ULL01-3	apatite	8.8	0.53	1.5	2.6	110.9	2.6	1.73	0.1	2.08	0.65	43.12

ULL01-4	apatite	3.7	0.22	2.2	3.2	88.9	3.4	1.43	0.0	2.27	0.67	45.60
ULL01-5	apatite	2.2	0.13	0.3	1.6	20.9	0.7	6.42	0.0	1.10	0.54	32.88
ULL01-6	apatite	6.1	0.36	4.0	14.0	154.7	8.0	3.51	0.2	2.73	0.68	48.12
ULL01-8	apatite	5.5	0.33	2.1	7.3	156.7	4.6	3.47	0.1	3.44	0.71	53.69
VIL01-1	apatite	6.6	0.40	1.7	6.5	83.3	3.6	3.86	0.08474	1.48	0.61	38.85
VIL01-2	apatite	6.2	0.37	2.1	14.2	173.1	6.2	6.77	0.15694	2.94	0.68	49.22
VIL01-3	apatite	6.4	0.39	2.4	4.2	84.2	3.8	1.71	0.07813	0.96	0.55	32.23
VIL01-4	apatite	7.9	0.47	4.0	15.3	136.8	8.2	3.86	0.23913	2.47	0.64	43.53
VIL01-5	apatite	2.3	0.14	2.0	14.0	92.4	5.6	7.15	0.03411	0.45	0.45	26.42
VILE07-1	apatite	3.9	0.24	1.5	4.2	77.1	2.9	2.75	0.0	5.63	0.73	57.33
VILE07-3	apatite	6.3	0.38	1.3	1.8	76.3	2.1	1.42	0.1	7.22	0.75	63.64
VILE07-4	apatite	2.4	0.14	1.6	3.6	82.9	2.9	2.18	0.0	9.26	0.77	67.88
VILE07-6	apatite	15.9	0.96	16.7	32.9	370.0	26.1	1.97	1.3	0.89	0.56	33.18
VILE07-8	apatite	9.2	0.55	1.4	3.0	96.3	2.6	2.11	0.1	3.90	0.72	56.12

Appendix E: Zircon U-Pb Geochronology Metadata

Compiled detrital zircon U-Pb geochronologic data for all Villicum and Ullum samples available as separate file upon request: plonka@unlv.nevada.edu.

REFERENCES

Allmendinger, R.W., and Judge, P.A., 2014, The argentine precordillera: A foreland thrust belt proximal to the subducted plate: Geosphere, v. 10, p. 1203–1218, doi:10.1130/GES01062.1.

Allmendinger, R.W., Figueroa, D., Snyder, D., Beer, J., Mpodozis, C., and Isacks, B.L., 1990, Foreland shortening and crustal balancing in the Andes at 30S Latitude: Tectonics, v.9, p. 789-809.

Allmendinger, R. W., Cardozo, N., and Fisher, D., 2012, Structural geology algorithms: Vectors and tensors in structural geology: Cambridge University Press (book to be published in early 2012).

Alvarado, P., Pardo, M., Gilbert, H., Miranda, S., Anderson, M., Saez, M., & Beck, S., 2009, Flat-slab subduction and crustal models for the seismically active Sierras Pampeanas region of Argentina: In S. M. Kay, V. A. Ramos, & W. R. Dickinson (Eds.), Backbone of the Americas: Shallow subduction, plateau uplift, and ridge and terrane collision, v. 204, p. 261–278, CO, USA: Geological Society of America Memoir. https://doi.org/10.1130/2009.1204(12).

Amidon, W. H., Fisher, G. B., Burbank, D. W., Ciccioli, P. L., Alonso, R. N., Gorin, A. L., et al., 2017, Mio-pliocene aridity in the south-central Andes associated with Southern Hemisphere cold periods. Proceedings of the National Academy of Sciences of the United States of America. 114, 6474–6479. doi: 10.1073/pnas.1700327114

Astini, R.A., Benedetto, J.L., and Vaccari, N.E., 1995, The early Paleozoic evolution of the Argentine Precordillera as a Laurentian rifted, drifted, and collided terrane: a geodynamic

model: Geological Society of America Bulletin, v. 107, p. 253–273, doi:10.1130/0016-7606(1995)107<0253:TEPEOT>2.3.CO;2.

Ault, A., Gautheron, C., and King, G., 2019, Innovations in (U-Th)/He, fission-track, and trapped-charge thermochronometry with applications to earthquakes, weathering, surface-mantle connections, and growth and decay of mountains: Tectonics, v. 38:11, p. 3705-3739, doi: 10.1029/2018TC005312.

Bahlburg, H., Vervoort, J.D., Du Frane, S.A., Bock, B., Augustsson, C., and Reimann, C., 2009, Timing of crust formation and recycling in accretionary orogens: Insights learned from the western margin of South America: Earth-Science Reviews, v. 97, p. 215–241, doi:10.1016/j.earscirev.2009.10.006.

Barazangi, M., and Isacks, B.L., 1976, Spatial distribution of earthquakes and subduction of the Nazca plate beneath South America: Geology, v. 4, no. 11, p. 686–692. https://doi.org/10.1130/0091-7613(1976)4<686:SDOEAS>2.0.CO;2.

Barazangi, M., Iscacks, B.L., 1979, Subduction of the Nazca plate beneath Peru evidence from spatial distribution and earthquakes: Geophysical Journal of the Royal Astronomic Society, v. 57, p. 537-555.

Beer, J.A., 1990, Steady Sedimentation and Lithologic Completeness, Bermejo Basin, Argentina: The Journal of Geology, v. 98, p. 501-517. Doi: http://www.jstor.org/stable/30065610

Beer, J.A, and Jordan, T.E., 1989, The effects of Neogene thrusting on deposition in the Bermejo Basin, Argentina: Journal of Sedimentary Research, v. 59, no. 2, p. 330-345. Doi: https://doi.org/10.1306/212F8F8A-2B24-11D7-8648000102C1865D.

Bellahsen, N., Sebrier, M., and Siame, L., 2016, Crustal shortening at the Sierra Pie de Palo (Sierras Pampeanas, Argentina): Near-surface basement folding and thrusting: Geological Magazine, v. 153, p. 992–1012, doi:10.1017/S0016756816000467.

Bercowski, F., Berenstein, L.R., and Johnson, N.M., 1987, Litofacies y Paleoambiente del Terciario en Lomas de las Tapias, Ullum, Prov. de San Juan, Argentina: Decimo congreso geologico Argentino, San Miguel de Tucuman, Actas II: p 101-104.

Boyce, J.W., and Hodges, K.V., 2005, U and Th zoning in Cerro de Mercado (Durango, Mexico) fluorapatite: Insights regarding the impact of recoil redistribution of radiogenic 4He on (U-Th)/He thermochronology: Chemical Geology, v. 219, p. 261-274, https://doi.org/10.1016/j.chemgeo.2005.02.007.

Buelow, E.K., Surian, J., Mahoney, J.B., Kimbrough, D.L., Mescua, J.F., Giambiagi, L.B., and Hoke, G.D., 2018, Sedimentologic and stratigraphic evolution of the Cachueta basin: Constraints on the development of the Miocene retroarc foreland basin, south-central Andes: Lithosphere, v. 10, no. 3, p. 366-391, https://doi.org/10.1120/L709.1.

Capaldi, T.N., Horton, B.K., McKenzie, N.R., Stockli, D.F., and Odlum, M.L., 2017, Sediment provenance in contractional orogens: The detrital zircon record from modern rivers in the Andean fold-thrust belt and foreland basin of western Argentina: Earth and Planetary Science Letters, v. 479, p. 83–97, https:// doi .org /10 .1016 /j .epsl .2017 .09 .001.

Capaldi, T.N., Horton, B.K., McKenzie, N.R., Mackaman-Lofland, C., Stockli, D.F., Ortiz, G., and Alvarado, P., 2020, Neogene Retroarc Foreland Basin Evolution, Sediment Provenance,

and Magmatism in Response to Flat Slab Subduction, Western Argentina: Tectonics, v. 39, p. 1–29, doi:10.1029/2019TC005958.

Capaldi, T.N., McKenzie, N.R., Horton, B.K., Mackaman-Lofland, C., Colleps, C.L., and Stockli, D.F., 2021, Detrital zircon record of Phanerozoic magmatism in the southern Central Andes: Geosphere, v. 17, p. 876–897, doi:10.1130/ges02346.1.

Casquet, C., Baldo, E., Pankhurst, R.J., Rapela, C.W., Galindo, C., Fanning, C.M., and Saavedra, J., 2001, Involvement of the Argentine Precordillera terrane in the Famatinian mobile belt: U-Pb SHRIMP and metamorphic evidence from Sierra Pie de Palo: Geology, v. 29, no. 8, p 703-706.

Ciccioli, P.L., Marenssi, S.A., Amidon, W.H., Limarino, C.O., and Kylander-Clark, A., 2018, Alluvial to lacustrine sedimentation in an endorheic basin during the Mio-Pliocene: The Toro Negro Formation, Central Andes of Argentina: Journal of South American Earth Sciences, v. 84, p. 69-87.

Coira, B.L., Davidson, J.D., Mpodozis, C., and Ramos, V.A., 1982, Tectonic and magmatic evolution of the Andes of northern Argentina and Chile: Earth-Science Reviews, v. 18, p. 303–332, https:// doi .org /10 .1016 /0012 -8252 (82)90042 -3.

Collo, G., Davila, F., Teixeira, W., Nobile, J.C., Sant'Anna, L.G., and Carter, A., 2017, Isotopic and thermochronologic evidence of extremely cold lithosphere associated with a slab flattening in the Central Andes of Argentina: Basin Research, v. 29, p. 16-40, doi:10.1111/bre.12162.

Contreras, V.H., Bracco, A.I., Baraldo, and J.A., 2019, Estratigrafia, bioestratigrafia y cronologia del Mioceno superior de la provincia de San Juan (Argentina): Opera lilloana 52: Mioceno al Pleistoceno del centro y norte de Argentina, p177-206.

Coutts, D., Matthews, W.A., and Hubbard, S.M., 2019, Assessment of widely used methods to derive depositional ages from detrital zircon populations: Geoscience Frontiers, v. 10, no. 4, p. 1421-1435, https://doi.org/10.1016/j.gsf.2018.11.002.

Cristallini, E.O., and Ramos, V.A., 2000, Thick-skinned and thin-skinned thrusting in the La Ramada fold and thrust belt: Crustal evolution of the High Andes of San Juan, Argentina (32°SL): Tectonophysics, v. 317, p. 205–235, doi:10.1016/S0040-1951(99)00276-0.

DeCelles, P.G., and Burden, E.T., 1992, Non-marine sedimentation in the overfilled part of the Jurassic-Cretaceous Cordilleran foreland basin: Morrison and Cloverly Formations, central Wyoming, USA: Basin Research, v. 4, p. 291-314, https://doi.org/10.1111/j.1365-2117.1992.tb00050.x.

DeCelles, P.G., and Giles, K.A., 1996, Foreland basin systems: Basin Research, v. 8, no. 2, p. 105–123, https:// doi .org /10 .1046 /j .1365 -2117 .1996 .01491 .x.

DeCelles, P.G., Gehrels, G.E., Quade, J., Ojha, T.P., Kapp, P.A., and Upreti, B.N., 1998, Neogene foreland basin deposits, erosional unroofing, and the kinematic history of the Himalayan fold-thrust belt, western Nepal: Geological Society of America Bulletin, v. 110 (1), p. 2–21. doi: https://doi.org/10.1130/0016-7606(1998)110<0002:NFBDEU>2.3.CO;2.

Del Rey, A., Deckart, K., Arriagada, C., and Martínez, F., 2016, Resolving the paradigm of the late Paleozoic–Triassic Chilean magmatism: Isotopic approach: Gondwana Research, v. 37, p. 172–181. https://doi.org/10.1016/j.gr.2016.06.008.

Dickinson, W. R., and Gehrels, G. E., 2009, Use of U–Pb ages of detrital zircons to infer maximum depositional ages of strata: A test against a Colorado plateau Mesozoic database: Earth and Planetary Science Letters, v. 288(1–2), p. 115–125. https://doi.org/10.1016/j.epsl.2009.09.013.

Ducea, M.N., Otamendi, J.E., Bergantz, G., Stair, K.M., Valencia, V.A., and Gehrels, G., 2010, Timing constraints on building an intermediate plutonic arc crustal section: U-Pb zircon geochronology of the Sierra Valle Fertil–La Huerta, Famatinian arc, Argentina: Tectonics, v. 29, TC4002, https://d oi. org/10 .1029 /2009TC002615.

Elhers, T.A., and Farley, K.A., 2003, Apatite (U-Th)/He thermocrhonometry: methods and applications to problems in tectonic and surface processes: Earth and Planetary Science Reviews, v. 206, p. 1-14. https://doi.org/10.1016/S0012-821X(02)01069-5.

Farley, K.A., 2000, Helium diffusion from apatite: General behavior as illustrated by Durango fluorapatite: Journal of Geophysical Research: Solid Earth, v. 105, no. B2, p. 2903-2914.

Farley, K.A., 2002, (U-Th)/He Dating: Techniques, Calibrations, and Applications: Reviews in Mineralogy and Geochemistry, v. 47(1), p. 819-844, DOI:10.2138/rmg.2002.47.18.

Fernandez, A.E., and Jordan, T.E., 1996, Analysis of controls on foreland basin stratigraphy using seismic and outcrop data: Application to the Bermejo basin, Central Andes, Argentina: XIII

Congreso Geologico Argentino y III Congreso de exploracion de hidrocarburos, Actas I: 373-383

Flemings, P.B., and Jordan, T.E., 1989, A Synthetic Stratigraphic Model of Foreland Basin Development: Journal of Geophysical Research, v. 94, p. 3851-3866, http://dx.doi.org/10.1029/JB094iB04p03851.

Flowers, R.M., Ketcham, R.A., Shuster, D.L., and Farley, K.A., 2009, Apatite (U-Th)/He thermochronometry using a radiation damage accumulation and annealing model: Geochimica et Cosmochimica, Acta 73, p. 2347-2365.

Fosdick, J.C., Grove, M., Graham, S.A., Hourigan, J.K., Lovera, O., and Romans, B.W., 2014, Detrital thermochronologic record of burial heating and sediment recycling in the Magallanes foreland basin, Patagonian Andes: Basin Research, v. 27, p. 546–572, doi:10.1111/bre.12088.

Fosdick, J.C., Carrapa, B., and Ortíz, G., 2015, Faulting and erosion in the Argentine Precordillera during changes in subduction regime: Reconciling bedrock cooling and detrital records: Earth and Planetary Science Letters, v. 432, p. 73–83, doi:10.1016/j.epsl.2015.09.041.

Fosdick, J.C., Reat, E.J., Carrapa, B., Ortiz, G., and Alvarado, P.M., 2017, Retroarc basin reorganization and aridification during Paleogene uplift of the southern central Andes: Tectonic, v. 36, p. 493-514, doi.10.1002/2016TC004400.

Furque, G., Gonzalez, P., Caballe, M., Perez, L., Cardo, R., Godeas, M., Conde, A., and Pucci, J.C, 2003, Hoja Geológica 3169-II, San José de Jáchal. Provincias de San Juan y La Rioja. Instituto de Geología y Recursos Minerales, Servicio Geológico Minero Argentino: Boletín 259- 76 p. Buenos Aires.

Garzanti, E., Capaldi, T.N., Tripaldi, A., Zarate, M., Vezzoli, G., and Limonta, M., 2022, Andean retroarc-basin dune fields and Pampean Sand Sea (Argentina): Provenance and drainage changes driven by tectonics and climate: Earth-Science Reviews, v. 231(4), DOI:10.1016/j.earscirev.2022.104077.

Gehrels, G., 2014, Detrital zircon U-Pb geochronology applied to tectonics: Annual Review of Earth and Planetary Sciences, V. 42, p 127-149, https://doi.org/10.1146/annurev-earth-0502120124012.

González Bonorino, F., 1950, Algunos problemas geológicos de las Sierras Pampeanas: Revista de la Asociación Geológica Argentina, v 5(3), p 81–110.

Haschke, M., Günther, A., Melnick, D., Echtler, H., Reutter, K.J., Scheuber, E., and Oncken, O., 2006, Central and southern Andean tectonic evolution inferred from arc magmatism, in Oncken, O., et al., eds., The Andes: Frontiers in Earth Sciences: Berlin, Springer, p. 337–353, https:// doi .org /10 .1007/978 -3 -540 -48684 -8_16.

Hervé, F., Fanning, C. M., Calderon, M., and Mpodozis, C., 2014, Early Permian to late Triassic batholiths of the Chilean frontal cordillera (28-31 S): SHRIMP U-Pb zircon ages and Lu-Hf and O isotope systems: Lithos, v. 184-187, p. 436–446. https://doi.org/10.1016/j. Lithos.2013.10.018.

Horton, B.K., and DeCelles, P.G., 2001, Modern and ancient fluvial megafans in the foreland basin systems of the central Andes, southern Bolivia: implications for drainage network evolution in fold-thrust belts: Basin Research, v. 13, p. 43-63.

Horton, B. K., and Schmitt, J. G., 1996, Sedimentology of a lacustrine fan-delta system, Miocene horse camp formation, Nevada, USA: Sedimentology, v. 43, p. 133–155. https://doi.org/10.1111/j.1365-3091.1996.tb01464.x.

Horton, B.K., Capaldi, T.N., and Perez, N.D., 2022, The role of flat slab subduction, ridge subduction and tectonic inheritance in Andean deformation: Geology, v. XX, https://doi.org/10.1130/G50094.1.

Jackson, S.E., Pearson, N.J., Griffin, W.L., and Belousova, E.A., 2004, The application of laser ablation–inductively coupled plasma–mass spectrometry to in situ U-Pb zircon geochronology: Chemical Geology, v. 211, p. 47–69, https://doi. org /10.1016/j.chemgeo.2004.06.017.

Johnson, N., Jordan, T., Johnsson, P., and Naser, C., 1986, Magnetic polarity stratigraphy, age and tectonic setting of fluvial sediments in an eastern Andean foreland basin, San Juan Province, Argentina: Foreland Basins (1986), p. 63-75.

Jones, R.E., Kirstein, L.A., Kasemann, S.A., Litvak, V.D., Poma, S., Alonso, R.N., and Hinton, R., 2016, The role of changing geodynamics in the progressive contamination of Late Cretaceous to late Miocene arc magmas in the southern Central Andes: Lithos, v. 262, p. 169–191, https:// doi .org /10.1016 /j .lithos .2016 .07 .002.

Jordan, T.E., and Allmendinger, R.W., 1986, The Sierras Pampeanas of Argentina; a modern analogue of Rocky Mountain foreland deformation: American Journal of Science, v. 286, p. 737–764, doi:10.2475/ajs.286.10.737.

Jordan, T. E., Isacks, B. L., Allmendinger, R. W., Brewer, J. A., Ramos, V. A., & Ando, C. J., 1983, Andean tectonics related to geometry of subducted Nazca plate: Geological Society of America Bulletin, v. 94, no. 3, p. 341–361, https://doi.org/10.1130/0016-7606(1983)94<341:ATRTGO>2.0.CO;2.

Jordan, T.E., Rutty, P.M., McRae, L.E., Beer, J.A., Tabbutt, K., and Damanti, J.F., 1990, Magnetic polarity stratigraphy of the miocene rio Azul section, precordillera thrust belt, san juan province, Argentina: The Journal of Geology, v. 98, p. 519-539, https://doi.org/10.1086/629422.

Jordan, T.E., Allmendinger, R.W., Damanti, J.F., and Drake, R.E., 1993, Chronology of Motion in a Complete Thrust Belt: The Precordillera, 30-31S, Andes Mountains: The Journal of Geology, Vol. 101, pp 135-156.

Jordan, T.E., Reynolds, J.H., and Erikson, J.P., 1997, Variability in age of initial shortening and uplift in the Central Andes, 16-33S, In: Ruddiman, W. (Ed.). Tectonic Uplift and Climate Change, Plenum Press, New York, pp. 41-61.

Jordan, T.E., Schlunegger, F., and Cardozo, N., 2001, Unsteady and spatially variable evolution of the Neogene Andean Bermejo foreland basin, Argentina: Journal of South American Earth Sciences, v. 14, p. 775-798.

Kay, S.M., and Abbruzzi, J.M., 1996, Magmatic evidence for Neogene lithospheric evolution of the central Andean “flat-slab” between 30S and 32 S: Tectonophysics, v 259, p. 15-28, doi: 10.1016/0040-1951(96)00032-7.

Kay, S.M., and Coira, B.L., 2009, Shallowing and steepening subduction zones, continental lithospheric loss, magmatism, and crustal flow under the central Andean Altiplano-Puna Plateau, in Kay, S.M., Ramos, V.A., and Dickinson, W.R., eds., Backbone of the Americas: Shallow Subduction, Plateau Uplift, and Ridge and Terrane Collision: Geological Society of America Memoir 204, p. 229-260, doi: 10.1130/2009.1204(11).

Kay, S. M., and Mpodozis, C., 2001, Magmatism as a probe to the Neogene shallowing of the Nazca plate beneath the modern Chilean flat- slab: Journal of South American Earth Sciences, v. 15, p. 39–57. https://doi.org/10.1016/s0895-9811(02)00005-6.

Kay, S.M., Mpodozis, C., Ramos, V.A., and Munizaga, F., 1991, Magma source variations for mid-late Tertiary magmatic rocks associated with a shallowing subduction zone and a thickening crust in the central Andes (28 to 33°S), in Harmon, R.S., and Rapela. C.W., eds., Andean Magmatism and its Tectonic Setting: Geological Society of America Special Paper 265, p. 113–137, https:// doi .org /10 .1130 /SPE265 -p113.

Keller, M., 1999, Argentine Precordillera: Sedimentary and plate tectonic history of a Laurentian crustal fragment in South America: Geological Society of America, v. 341, 1–131 p., doi:10.1130/0-8137-2341-8.1.

Kleiman, L.E., and Japas, M.S., 2009, The Choiyoi volcanic province at 34°S–36°S (San Rafael, Mendoza, Argentina): Implications for the late Paleozoic evolution of the southwestern margin of Gondwana: Tectonophysics, v. 473, no. 3–4, p. 283–299, https:// doi .org /10 .1016 /j .tecto .2009 .02.046.

Lacombe, O., and Bellahsen, N., 2016, Thick-skinned tectonics and basement-involved fold-thrust belts: Insights from selected Cenozoic orogens: Geological Magazine, v. 153, 763–810 p., doi:10.1017/S0016756816000078.

Lawton, T.F., Schellenbach, W.L., and Nugent, A.E., 2014, Late Cretaceous fluvial-megafan and axial river systems in the southern cordilleran foreland basin: drip tank member of straight cliffs formation and adjacent strat, Southern Utah, U.S.A: Journal of Sedimentary Research, v. 84, p. 407-434, doi:10.2110/jsr.2014.33.

Levina, M., Horton, B.K., Fuentes, F., and Stockli, D.F., 2014, Cenozoic sedimentation and exhumation of the foreland basin system preserved in the Precordillera thrust belt (31-32°S), southern central Andes, Argentina: Tectonics, v. 33, p. 1659–1680, doi:10.1002/2013TC003424.

Limarino, C., Tripalid, A., Marenssi, S., Net, L., Re, G., and Caselli, A., 2001, Tectonic controls on the evolution of fluvial systems of the Vinchina Formation (Miocene), northwestern Argentina: Journal of South American Earth Sciences, v. 14, p. 751-762.

Löbens, S., Bense, F.A., Dunkl, I., Wemmer, K., Kley, J., and Siegesmund, S., 2013, Thermochronological constraints of the exhumation and uplift of the Sierra de Pie de Palo, NW Argentina: Journal of South American Earth Sciences, v. 48, p 209-219.

Lossada, A. C., Giambiagí, L., Hoke, G. D., Fitzgerald, P. G., Creixell, C., Murillo, I., Mardonez, D., Velasquez, R., and Suriano, J., 2017, Thermochronologic evidence for late Eocene Andean mountain building at 30°S: Tectonics, 36, 2693–2713. https://doi.org/10.1002/2017TC004674.

Mackaman-Lofland, C., Horton, B.K., Fuentes, F., Constenius, K.N., Ketcham, R.A., Capaldi, T.N., Stockli, D.F., Ammirati, J.B., Alvarado, P., and Orozco, P., 2020, Andean Mountain Building and Foreland Basin Evolution During Thin- and Thick-Skinned Neogene Deformation (32–33°S): Tectonics, v. 39, p. 1–27, doi:10.1029/2019TC005838.

Mackaman-Lofland, C., Horton, B.K., Ketcham, R.A., McQuarrie, N., Fosdick, J.C., Fuentes, F., Constenius, K.N., Capaldi, T.N., Stockli, D.F., and Alvarado, P., 2022, Causes of Variable Shortening and Tectonic Subsidence During Changes on Subduction: Insights from Flexural Thermokinematic Modeling of the Neogene Southern Central Andes (28-30S): Tectonics, v. 41, https://doi.org/10.1029/2022tc007334.

Maksaev, V., Munizaga, F., and Tassinari, C., 2014, Timing of the magmatism of the paleo-Pacific border of Gondwana: U-Pb Geochronology of Late Paleozoic to Early Mesozoic igneous rocks of the north Chilean Andes between 20 and 30S: Andean Geology, v. 41, p. 447-506, doi:10.5027/andgeoV41n3-a01.

Malizia, D.C., Reynolds, J.H., and Tabbutt, K., 1995, Cronología de la sedimentacion Neogena, tectonismo y edad de la estructuracion en el Campo de Talampaya, pp. 78-105.

Mardonez, D., Suriano, J., Giambiagi, L., Mescua, J., Lossada, A., Creixell, C., and Murillo, I., 2020, The Jachal river cross-section revisited (Andes of Argentina, 30 S): Constraints from the chronology and geometry of neogene synorogenic deposits: Journal of South American Earth Sciences, v.104, https://doi.org/10/1016/j.jsames.2020.102838.

Martin, E.L., Collins, W.J., and Spencer, C.J., 2019, Laurentian origin of the Cuyania suspect terrane, western Argentina, confirmed by Hf isotopes in zircon: Geological Society of America Bulletin, v. 132, p. 273–290, https:// doi .org /10 .1130/B35150 .1.

Meigs, A., Krugh, W.C., Schiffman, C., Verges, J., and Ramos, V.A., 2006, Refolding of the thin-skinned thrust sheers by active basement-involved thrust faults in the Eastern Precordillera of Western Argentina: Revista de la Asociacion Geologica Argentina, 61, p. 589-603

Miall, A.D., 1977, Lithofacies Types and Vertical Profile Models in Braided River Deposits: A Summary: In: Miall, A.D., Ed., Fluvial Sedimentology, Geological Survey of Canada, Calgary, p. 597-604.

Milana, J. P., Bercowski, F., and Jordan, T. E., 2003, Paleoambientes y magnetoestrigrafía del Neógeno de la Sierra de Mogna, y su relación con la Cuenca de Antepaís Andina. Revista de la Associacion Geologica Argentina, 38, 447–473.

Mpodozis, C., and Kay, S.M., 1992, Late Paleozoic to Triassic evolution of the Gondwana margin: evidence from Chilean Frontal cordilleran batholiths (28°S to 31°S): Geological Society of America Bulletin, v. 104, p. 999–1014, doi:10.1130/0016-7606(1992)104<0999:LPTTEO>2.3.CO;2.

Mulcahy, S.R., Roeske, S.M., McClelland, W.C., Jourdan, F., Iriondo, A., Renne, P.R., Vervoort, J.D., and Vujovich, G.I., 2011, Structural evolution of a composite middle to lower crustal section: The Sierra de Pie de Palo, northwest Argentina: Tectonics, v. 30, doi.10.1029/2009TC002656.

Mulcahy, S.R., Roeske, S.M., McClelland, W.C., Ellis, J.R., Jourdan, F., and Renne, P.R., 2014, Multiple migmatite events and cooling from granulite facies metamorphism within the Famatina arc margin of Northwest Argentina: Tectonics, v. 33, p. 1–25. https://doi.org/10.1002/2013TC003398.

Nemec, W., and Steel, R. J., 1984, Alluvial and coastal conglomerates: Their significant features and some comments on gravelly mass-flow deposits: In Sedimentology of gravels and conglomerates, v. 10, p. 1–31, Alberta, Canada: Canadian Society of Petroleum Geologists Memoir.

Ortiz, G., Alvarado, P., Fosdick, J.C., Perucca, L., Saez, M., and Venerdini, A., 2015, Active deformation in the northern Sierra de Valle Fértil, Sierras Pampeanas, Argentina: Journal of South American Earth Sciences, v. 64, p. 339–350, doi:10.1016/j.jsames.2015.08.015.

Ortiz, G., Stevens Goddard, A.L., Fosdick, J.C., Alvarado, P., Carrapa, B., and Cristofolini, E., 2021, Fault reactivation in the Sierras Pampeanas resolved across Andean extensional and compressional regimes using thermochronolgic modeling: Journal of South American Earth Sciences, v. 112, https://doi.org/10.1016/j.jsames.20210103533.

Otamendi, J.E., Ducea, M.N., Cristofolini, E.A., Tibaldi, A.M., Camilletti, G.C., and Bergantz, G.W., 2017, U-Pb ages and Hf isotope compositions of zircons in plutonic rocks from the central Famatinian arc, Argentina: Journal of South American Earth Sciences, v. 76, p. 412–426, https://doi.org/10.1016/j.jsames.2017.04.005.

Paces, J.B. and Miller, J.D., 1993, Precise U-Pb Ages of Duluth Complex and Related Mafic Intrusions, Northeastern Minnesota: Geochronological Insights to Physical, Petrogenic,

Paleomagnetic and Tectonomagmatic Processes Associated with the 1.1 Ga Midcontinent Rift System: Journal of Geophysical Research: Solid Earth, v. 98, p. 13997-14013. http://dx.doi.org/10.1029/93JB01159.

Parker, S.D., and Pearson, D.M., 2021, Pre-Thrusting Stratigraphic Control on the Transition From a Thin-Skinned to Thick-Skinned Structural Style: An Example From the Double-Decker Idaho-Montana Fold-Thrust Belt: Tectonics, v. 40, doi:10.1029/2020TC006429.

Paton, C., Hellstrom, J., Paul, B., Woodhead, J., and Hergt, J., 2011, Iolite: Freeware for the visualization and processing of mass spectrometric data: Journal of Analytical Atomic Spectrometry, v. 26, p. 2508-2518.

Perez, N. D., and Horton, B. K., 2014, Oligocene-Miocene deformational and depositional history of the Andean hinterland basin in the northern Altiplano plateau, Southern Peru: Tectonics, v. 33, p. 1819–1847. https://doi.org/10.1002/2014TC003647.

Petrus, J.A., and Kamber, B.S., 2012, VizualAge: A Novel Approach to Laser Ablation ICP-MS U-Pb Geochronology Data Reduction: Geostandards and Geoanalytical Research, v. 36, p. 247-270.

Pinto, L., Alarcón, P., Morton, A., & Naipauer, M., 2018, Geochemistry of heavy minerals and U–Pb detrital zircon geochronology in the Manantiales Basin: Implications for frontal cordillera uplift and foreland basin connectivity in the Andes of Central Argentina: Palaeogeography, Palaeoclimatology, Palaeoecology, 492, 104–125. https://doi.org/10.1016/j.palaeo.2017.12.017.

Podesta, M., Ortiz, G., Orozco, P., Alvarado, P., and Fuentes, F., 2022, The Iglesia basin (San Juan, Argentina), seismic interpretation, geometry basin, and implications for geothermal systems: Andean Geology, v. 39, no. 3, doi:10.5027/andgeoV49n3-3340.

Ramos, V.A., 2004, Cuyania, an exotic block to Gondwana: Review of a historical success and the present problems: Gondwana Research, v. 7, p. 1009–1026, https:// doi .org /10.1016 /S1342 -937X (05)71081 -9.

Ramos, V.A., 2009, Anatomy and global context of the Andes: Main geologic features and the Andean orogenic cycle, in Kay, S.M., Ramos, V.A., and Dickinson, W.R., eds., Backbone of the Americas: Shallow Subduction, Plateau Uplift, and Ridge and Terrane Collision: Geological Society of America Memoir 204, p. 31–65, https:// doi .org /10 .1130 /2009 .1204 (02).

Ramos, V. A., and Folguera, A., 2009, Andean flat-slab subduction through time: Geological Society, London, Special Publications, v. 327, p. 31–54. https://doi.org/10.1144/SP327.3.

Ramos, V.A., Jordan, T.E., Allmendinger, R.W., Kay, S.M., Cortes, J.M., and Palma, M., 1986, Paleozoic terranes of the central Argentine-Chilean Andes: Tectonics, v. 5, p. 855–880, https://doi .org /10 .1029 /TC005i006p00855.

Ramos, V.A., Cristallini, E.O., and Pérez, D.J., 2002, The Pampean flat-slab of the Central Andes: Journal of South American Earth Sciences, v. 15, p. 59–78, doi:10.1016/S0895-9811(02)00006-8.

Rapela, C.W., Verdecchia, S.O., Casquet, C., Pankhurst, R.J., Baldo, E.G., Galindo, C., Murra, J.A., Dahlquist, J.A., and Fanning, C.M., 2016, Identifying Laurentian and SW Gondwana

sources in the Neoproterozoic to early Paleozoic metasedimentary rocks of the Sierras Pampeanas: Paleogeographic and tectonic implications: Gondwana Research, v. 32, p. 193–212, https:// doi .org /10 .1016 /j .gr .2015 .02 .010.

Rapela, C.W., Pankhurst, R.J., Casquet, C., Dahlquist, J.A., Fanning, C.M., Baldo, E.G., Galindo, C., Alasino, P.H., Ramacciotti, C.D., Verdecchia, S.O., and Murra, J.A., 2018, A review of the Famatinian Ordovician magmatism in southern South America: Evidence of lithosphere reworking and continental subduction in the early proto-Andean margin of Gondwana: Earth-Science Reviews, v. 187, p. 259–285, https:// doi .org /10.1016 /j .earscirev .2018 .10 .006.

Rimando, J.M., and Schoenbohm, L.M., 2020, Regional relative tectonic activity of structures in the Pampean flat slab segment of Argentina from 30 to 32 S: Geomorphology, v. 350, https://doi.org/10.1016/j.geomorph.2019.106908.

Rubatto, D., 2017, Zircon: The Metamorphic Mineral: Reviews in Mineralogy & Geochemistry, v. 83, p. 261-295, http://dx.doi.org/10.2138/rmg.2017.83.09.

Sato, A.M., Llambías, E.J., Basei, M.A., and Castro, C.E., 2015, Three stages in the late Paleozoic to Triassic magmatism of southwestern Gondwana, and the relationships with the volcanogenic events in coeval basins: Journal of South American Earth Sciences, v. 63, p. 48–69, https:// doi .org /10.1016 /j .jsames .2015 .07 .005.

Saylor, J. E., Jordan, J. C., Sundell, K. E., Wang, X., Wang, S., and Deng, T., 2018, Topographic growth of the Jishi Shan and its impact on basin and hydrology evolution, NE Tibetan Plateau. Basin Research, v. 30, 544–563. doi: 10.1111/bre.12264.

Schmitz, M.D., and Bowring, S.A., 2001, U-Pb zircon and titanite systematics of the Fish Canyon Tuff: An assessment of high-precision U-Pb geochronology and its application to young volcanic rocks: Geochimica et Cosmochimica Acta, v. 65, p. 2571–2587, doi:10.1016/S0016-7037(01)00616-0.

Schwartz, J.J., Gromet, L.P., and Miro, R., 2008, Timing and duration of the calc-alkaline arc of the Pampean orogeny: Implications for the late Neoproterozoic to Cambrian evolution of western Gondwana: The Journal of Geology, v. 116, p. 39–61, https:// doi .org /10 .1086 /524122.

Shuster, D.L., Flowers, R.M., and Farley, K.A., 2006, The influence of natural radiation damage on helium diffusion kinetics in apatite: Earth and Planetary Science Letters, v. 249, p. 148-161.

Siame, L.L., Bellier, O., Sebrier, M., Bourles, D.L., Leturmy, P., Perez, M., and Araujo, M., 2002, Seismic hazard reappraisal from combined structural geology, geomorphology and cosmic ray exposure dating analyses: The Eastern Precordillera thrust system (NW Argentina): Geophysical Journal International, v. 150, p. 241-260.

Siame, L.L., Bellier, O., Sébrier, M., and Araujo, M., 2005, Deformation partitioning in flat subduction setting: Case of the Andean foreland of western Argentina (28°S-33°S): Tectonics, v. 24, p. 1–24, doi:10.1029/2005TC001787.

Sláma, J. et al., 2008, Plešovice zircon - A new natural reference material for U-Pb and Hf isotopic microanalysis: Chemical Geology, v. 249, p. 1–35, doi:10.1016/j.chemgeo.2007.11.005.

Sobel, E.R., and Strecker, M.R., 2003, Uplift, exhumation and precipitation: Tectonic and climatic control of Late Cenozoic landscape evolution in the northern Sierras Pampeanas, Argentina: Basin Research, v. 15(4), p. 431-451, https://doi.org/10.1046/j.1365-2117.2003.00214.x.

Stevens-Goddard, A.L., Larrovere, M.A., Carrapa, B., Aciar, R.H., and Alvarado, P., 2018, Reconstructing the thermal and exhumation history of the sierras Pampeanas through low-temperature thermochronology: A case study from the sierra de Velasco: Geological Society of America Bulletin, v 130(11–12), p. 1842–1858. https://doi.org/10.1130/B31935.1.

Tholt, A., Mulcahy, S., McClelland, W.C., Roeske, S.M., Meira, V.T., Webber, P., Houlihan, E., Coble, M.A., and Vervoort, J.D., 2021, Metamorphism of the Sierra de Maz and implications for the tectonic evolution of the MARA terrane: Geosphere, https://doi.org/10.1130/GES02268.1.

Thomas, W.A., Astini, R.A., Mueller, P.A., and McClelland, W.C., 2015, Detrital-zircon geochronology and provenance of the Ocloyic synorogenic clastic wedge, and Ordovician accretion of the Argentine Precordillera terrane: Geosphere, v. 11, p. 1749–1769, doi:10.1130/GES01212.1.

Vergés, J., Ramos, E., Seward, D., Busquets, P., and Colombo, F., 2001, Miocene sedimentary and tectonic evolution of the Andean Precordillera at 31°S, Argentina: Journal of South American Earth Sciences, v. 14, no. 7, p. 735–750. https://doi.org/10.1016/S0895-9811(01)00070-0.

Vergés, J., Ramos, V.A., Meigs, A., Cristallini, E., Bettini, F.H., and Cortés, J.M., 2007, Crustal wedging triggering recent deformation in the Andean thrust front between 31°S and 33°S:

Sierras Pampeanas-Precordillera interaction: Journal of Geophysical Research: Solid Earth, v. 112, p. 1–22, doi:10.1029/2006JB004287.

Vermeesch, P., 2018, IsoplotR: A free and open toolbox for geochronology: Geoscience Frontiers, v. 9, p. 1479-1493., https://doi.org/10.1016/j.gsf.2018.04.001.

Von Gosen, W., 1992, Structural evolution of the Argentine precordillera: the Rio San Juan section: Journal of Structural Geology, v. 14, p. 643–667, doi:10.1016/0191-8141(92)90124-F.

Yáñez, G.A., Ranero, C.R., Huene, R., and Díaz, J., 2001, Magnetic anomaly interpretation across the southern Central Andes (32–34 S): The role of the Juan Fernández ridge in the late tertiary evolution of the margin: Journal of Geophysical Research, v. 106(B4), p. 6325–6345. https://doi.org/10.1029/2000JB900337.

Yonkee, A., and Weil, A.B., 2015, Tectonic evolution of the Sevier and Laramide belts within the North American Cordilleran orogenic system: Earth-Science Reviews, v. 150, p. 531-593, https://doi.org/10.1016/j.earscirev.2015.02.001.

Zapata, T.R., and Allmendinger, R.W., 1996, Thrust-front zone of the Precordillera, Argentina: A thick-skinned triangle zone: American Association of Petroleum Geologists Bulletin, v. 80, p. 359–381, doi:10.1306/64ed87e6-1724-11d7-8645000102c1865d.

CURRICULUM VITAE

ZOEY PLONKA, M.S.
PLONKAZ@UMICH.EDU

Education

MS University of Nevada, Las Vegas — December, 2022
Geoscience
Thesis: *Along strike tectonic evolution of the Neogene Bermejo foreland basin and Eastern Precordillera thrust front, Argentina (30-32°S)*
Advisor: Tomas Capaldi

BS University of Michigan — December, 2019
Earth and Environmental Science

Honors and Awards/Grants/Scholarships

Natural Science Association Scholarship 2022

($1635)

Bernada French Scholarship 2021, 2022

($1000)

Nate Forrest Stout Memorial Scholarship 2021, 2022

($750)

Geological Society of America:
Graduate Student Research Grant 2021
($2500)

University Honors 2017-2019

Awarded to students with 3.5 or greater GPA

University of Michigan HAIL Scholar 2016-2019

($66000/4 years)

Jeanne Eckert Scholarship 2016

($1000)

Research Experience

Master's Thesis, University of Nevada, Las Vegas **2020-2022**
Advisor: Dr. Tomas Capaldi

- Utilized the sediment record to assess variations in retro-arc basin formation and thrust front evolution in a flat-slab subduction zone through:
    - Measuring two 2km thick stratigraphic sections, collecting samples, and compiling in-situ paleoflow and provenance datasets and observing general field relationships
    - Building new geo- and thermochronologic datasets using detrital minerals (zircon & apatite) to provide constraints on deposition, provenance, and exhumational related cooling over the past 20 Myr
    - In depth literature review and correlation of new datasets with published datasets along-strike to assess debated variations in thrust-front evolution, basin formation, and structural domains in an active flat-slab subduction and broken foreland environment

University of Michigan, Ann Arbor **2018-2019**
Lab Assistant under Dr. Nathan Sheldon

- Investigated carbon isotope fractionation in leaves, soils, and paleosols from the West/Southwestern United States to track paleoclimatic changes. Obtained isotope data to build correlations with elevation, mean annual temperature, mean annual precipitation and atmospheric carbon concentration
- Duties included cleaning samples through acidification processes, processing samples using Shatterbox and Jaw Crusher machinery, operating and performing maintenance on Elemental Analysis (EA) and Cavity Ring Down Spectroscopy (CRDS) machinery

Teaching and Work Experience

Kinross Gold Corporation, Round Mountain NV **June-September 2022**
Environmental Specialist Intern, Round Mountain Gold Mine

- Worked with the Environmental team as an intern through the Nevada Mining Association's 360 Internship Program
    - Assisted in the collection of water samples, conducting daily and monthly site inspections, and environmental permitting.
    - Completed a project updating the SRCE (Standardized Reclamation Cost Estimate) Model using AutoCAD software.

Bureau of Land Management, Caliente NV **May-June 2022**
Geology Intern, Caliente Field Office

- Worked with BLM Field Geologists as an intern through the Nevada Mining Association's 360 Internship Program
    - Assisted in conducting field inspections of active and inactive mineral exploration sites for permitting and bond-release.

- Gained experience reviewing active case files and plans of operation for mineral exploration in Lincoln County, Nevada.

University of Nevada, Las Vegas **January-May 2022**
Teaching Assistant, Geography 430: GIS: Theory and Application

- Instructed undergraduate students in the lab portion of this course following Mastering ArcGIS, 8th edition by Maribeth Price (Lab Manual).
  - Taught students to operate and troubleshoot ArcMap software to create, process, and visualize geospatial datasets.

University of Nevada, Las Vegas **January-May 2022**
Teaching Assistant, Geology 630-GIS: Theory and Application

- Instructed graduate students in the lab portion of this course following Mastering ArcGIS, 8th edition by Maribeth Price (Lab Manual).
  - Taught students to operate and troubleshoot the software to create, process, and visualize geospatial datasets.

University of Nevada, Las Vegas **August-December 2021**
Teaching Assistant, Geology 448: Field 1

- Helped lead 7 weekend mapping trips in southern Nevada
  - Instructed students on basic field geology skills including collecting field data (strike and dip measurements, detailed field notes/sketches), creating detailed geologic maps, and creating geologic cross-sections.

University of Nevada, Las Vegas **January-May 2021**
Teaching Assistant, Geology 362: Sedimentology and Stratigraphy

- Instructed undergraduate students in the lab portion of this class
  - Taught students the necessary skills to identify and interpret sedimentary rocks and structures.
  - Assisted with two field trips: instructed students how to measure stratigraphic section with a Jacob's staff, take detailed field notes, and interpret depositional environments.

University of Nevada, Las Vegas **August-December, 2020**
Teaching Assistant, Geology 448: Field 1

- Helped lead 5 weekend mapping trips near the Las Vegas Valley
  - Instructed students on basic field geology skills including collecting field data (strike and dip measurements, detailed field notes/sketches), creating detailed geologic maps, and creating geologic cross-sections.

Field Experience

- **Argentina, Nov-Dec 2022**
  - Assisted an M.S. student from the University of Texas at Austin with his Master's field work measuring and mapping Paleozoic stratigraphy near San Juan, Argentina
- **Gold Hill, UT, May 2022**
  - Assisted fellow M.S. student from the University of Nevada, Las Vegas on a portion of their Master's field work (~4 days)
  - Helped collect samples, operate GPS, identify minerals, and observe geologic field relationships.
- **Argentina, Nov-Dec 2021**
  - Spent four-weeks in the San Juan Province, Argentina observing/studying regional geology.
  - Measured ~2 km of Cenozoic basin stratigraphy, collected rock/sand samples for analyses, took in-field measurements of paleoflow on imbricated clasts, conducted in-field conglomerate clast counts, recorded detailed notes on field relationships.
  - Assisted in an elevation transect of basement structures in the region, collecting rock and sand samples for thermochronologic analyses
- **Southern Nevada, Fall 2020 & 2021**
  - Teaching assistant for Field Geology I: Helped scout mapping areas in the Eldorado Mountains, Muddy Mountains, and Calico Basin
  - Produced detailed geologic maps and cross sections for: Eldorado Mountains near Searchlight, NV; Muddy Mountains near Valley of Fire, NV; and Calico Basin
- **Inyo-White Mountains, CA, May 2021**
  - Produced detailed geologic maps and cross sections for the Poleta Folds region in the White Mountains of southern-eastern California (near Bishop, CA)
  - Mapped several Jurassic Plutons in the White-Inyo region (Papoose Flats and Sage Hen Flats, CA)
- **Jackson Hole, WY, July 2019**
  - Completed the four-week culminating field experience for geology undergraduates at University of Michigan
  - Produced detailed geologic maps and cross sections for several geologic regions near Jackson Hole, Wyoming (including the Red Hills near Grand Teton National Park and exposures in the Snake River Canyon)
  - Measured 300 meters of Jurassic-aged sedimentary stratigraphy

Presentations and Invited Lectures

Guest Lecture for Career Seminar in Earth and Environmental Sciences at Utah Tech University, September 2022, "Life as a Graduate Student & How I Got Here."

Plonka, Z.P., Capaldi, T.N., Odlum, M., Alvarado, P., and Ortiz, G., April 2022. Tracking the Neogene tectonic evolution of the active Andean thrust front using the foreland basin record and

detrital geo-/thermochronology, western Argentina (31-32ºS), UNLV Department of Geoscience Geosymposium, oral presentation.

Plonka, Z.P., Capaldi, T.N., Odlum, M., Alvarado, P., and Ortiz, G., March 2022. Tracking the Neogene tectonic evolution of the active Andean thrust front using the foreland basin record and detrital geo-/thermochronology, western Argentina (31-32ºS). Geological Society of America Cordilleran and Rocky Mountain Joint Section Meeting, oral presentation.

Oral Presentation to Collaborators in the Consejo Nacional de Investigaciones Científicas y Técnicas (CONICET) group at Universidad de San Juan Nacional, December 2021, Resolving Along-Strike Andean Thrust Front Evolution Using the Well-Preserved Neogene Foreland Basin Record in the Pampean Flat Slab Region of Argentina.

Plonka, Z.P., Capaldi, T.N., Oldum, M., Ortiz, G., and Alvarado, P., October 2021. Resolving Along-Strike Andean Thrust Front Evolution Using the Foreland Basin Record in the Flat Slab Region of Argentina. Geological Society of America Conference, poster presentation.

Plonka, Z.P., and Capaldi, T.N., April, 2021. Tectonic Evolution of the Eastern Precordillera using the broken foreland basin record. UNLV Department of Geoscience Geosymposium, poster presentation.

Professional Training

Mine Safety and Health Administration Training
Round Mountain Gold Corporation, Nevada, June 2022
Completed 24 hours of mandatory MSHA training at Kinross' Round Mountain Gold Corporation.

Professional Affiliations

Association for Women Geoscientists, 2020-Present
President of the UNLV student chapter (2021-2022). Led meetings, organized social events, organized community service events. Major accomplishments include organizing/leading a Resume/CV workshop and Virtual Geoscience Careers Seminar for undergraduate students in the Geosciences.

American Association of Petroleum Geologists, 2020-Present
Scheduling Liaison for the UNLV student chapter. Helped organize and lead community service events.

Society of Economic Geologists, 2021-Present
Member of international and UNLV student chapter. Helped organize and run a field trip to Ely, Nevada where we visited popular mineral collecting sites and toured the Robinson Mine in Ely (April, 2022).

Geological Society of Nevada, 2022

Geological Society of America, 2020-Present

Community Service and Organized Events

Women in Geoscience Career Seminar
Association for Women Geoscientists, December 1st 2022
Organized and hosted a virtual seminar which consisted of a panel of four women in various geoscience careers (academia, mineral industry, government, and consulting) to provide insight to UNLV and other Geoscience students on the opportunities for post-graduate careers.

Resume/CV Workshop
Association for Women Geoscientists, October 27th 2022
Organized and led a Resume/CV workshop for UNLV department of geoscience undergraduate students which acted as a space for students to have their resume, CV, short application, cover letter, &/or statement of purpose reviewed by graduate students and faculty.

Geoscience Field Day
Association for Women Geoscientists, September 2022
Organized and hosted (along with UNLV SEG) a Field Day event for UNLV Department of Geoscience students and staff as an opportunity to introduce the Geoscience clubs present on campus.

Nelson River Clean Up (Second annual)
Association for Women Geoscientists, May 2022
Organized and led a trash-clean up event at a popular, local swim/hike spot along the Colorado River.

Nelson River Clean Up (First annual)
Association for Women Geoscientists, April 2021
Helped organize and lead a trash-clean up event at a popular, local swim/hike spot along the Colorado River.

Community Outreach (Las Vegas)
Geoscience Department, February 2021
Participated as a panelist of geoscience graduate students and faculty for local high school students presenting science projects completed through their Geology and Geography course. Engaged with students and provided feedback on the scientific method.

Girls in Science and Engineering Camp Volunteer
Women in Science and Engineering, July 2018
Acted as Chemistry Student Mentor for the Girls in Science and Engineering Camp at the University of Michigan.

After School Program Tutor
Books for a Benefit, 2016-2017
Tutored 1st-12th grade students who attended an after-school program for low-income families.

Skills

Computer skills
Proficient in ESRI ArcGIS (Desktop and Online), Microsoft Office Suite, Adobe Creative Suite (Illustrator and Photoshop), Google Earth PRO. Experience using AutoCAD.

Lab Skills
Experience using rock crusher equipment, cleaning and processing samples, mineral separation (via water table), using petrographic and regular microscopes for mineral identification and picking. Assisted in the running of LA-ICP-MS (Laser ablation inductively coupled plasma mass spectrometer) to conduct geo/thermochronological analyses. Assisted in running and performing maintenance on Elemental Analysis and CRDS (Cavity ring down spectroscopy) machinery.

Field Skills
Ability to create detailed geologic maps and cross sections, measure and produce detailed stratigraphic sections, collect soil, sand, water, and rock samples. Experience mapping soil horizons.